Politecnico di Torino

Dipartimento di Ingegneria Meccanica e Aerospaziale

Laurea Magistrale in Ingegneria Aerospaziale

Academic Year 2024/2025

Setup and characterization of a wind tunnel for turbulence manipulation studies

Supervisors
Gioacchino Cafiero
Jacopo Serpieri
Edoardo Fracchia

Candidate
Gabriele Simone Pipino
317544

April 2025

To my family

Abstract

The development of flow control techniques aimed at reducing aerodynamic drag is a topic of significant interest within the fluid dynamics research community. Drag reduction is, in fact, a key factor in lowering the emissions and operating costs of transport vehicles. The portion of drag resulting from the viscous forces arising in the proximity of surfaces, referred to as skin friction, is particularly relevant in aerodynamic bodies such as aircraft wings and fuselages.
A promising passive flow control method that allows to reduce skin friction consists in applying microscopic-sized grooves, known as riblets, to the surface.
Experimental observations of riblet manipulated boundary layers are usually carried out on riblet equipped tiles installed within the surface of a bigger flat plate. The requirements for successfully conducting this type of experimental studies are thus that the flat plate flow is canonical, adhering to the zero pressure gradient condition, and that the boundary layer behaves correctly.
In this work, the last steps of the assembly of the recently renewed boundary layer observation facility of the Politecnico di Torino are covered. The experimental setup preparation involved the design of new components and solutions to enhance the facility's operating field, including different turbulence tripping devices and a terminal flap for pressure gradient management. The wind tunnel has also undergone a preliminary characterization, where the flow quality and the effect of the previously mentioned devices have been tested. Static pressure measurements through the flat plate pressure taps have been employed to study the effect of the flap on the pressure field, obtaining a map of the realizable operating conditions for different flow velocity and flap deflection combinations. Hot wire anemometry was used to carry out boundary layer observations in multiple positions along the flat plate at different velocities, applying two different types of turbulence tripping devices. The natural transition of the boundary layer was thus highlighted, and the development of the artificially generated turbulent boundary layers was examined. Recently proposed diagnostic approaches have been applied to the study of the behavior of the turbulent boundary layer.
This study therefore serves to test the reconfigured experimental facility, making sure that the previously introduced requirements are met while also comparing the experimental results with data from previous works.

Contents

List of Figures

List of Tables

Chapter 1

Introduction

The development of flow control techniques for drag reduction has been a major focus for researchers in the field of fluid dynamics. A large part of the energy consumed in key engineering applications, such as transportation and pipe systems is, in fact, used to overcome fluid dynamic drag.

1.1 What causes drag

In fluid dynamics, the force experienced by a solid body in opposition to its relative movement with respect to a fluid is referred to as drag or, often, as fluid resistance.
Drag is generally divided into two components:

- Pressure drag: the contribution to drag due to differential pressure, related to the body shape and, inherently, to its wake configuration
- Skin friction: the drag component due to the viscous forces acting mutually between the fluid and the body

The importance of one of these two components of the drag force with respect to the other is associated with "how aerodynamic" the body affected by the drag force is. In fluid dynamics, a body is defined as "aerodynamic" if its shape is streamlined, leading to a smaller wake and, as a consequence, a smaller pressure drag component. Conversely, bluff bodies are those for which pressure drag is the main component of fluid resistance, as a consequence of the development of a more significant wake.
In aeronautical applications, which generally involve aerodynamic bodies, the study of the mechanisms that drive and regulate skin friction production becomes, therefore, a topic of great interest.

The boundary layer

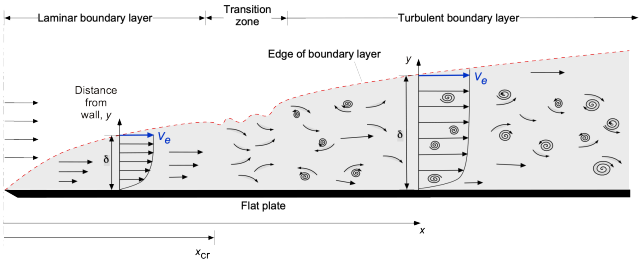

Figure 1.1: Representation of the boundary layer regimes

The boundary layer is the near-wall region where the flow velocity transitions from the free-stream value to zero, to comply with the no-slip condition. Since this region is inherently associated with viscous stresses, it is clear that the phenomena that govern skin friction production occur within it. The boundary layer characteristics depend on the flow regime and thus on the Reynolds number:

- **Laminar boundary layer:**
  At lower Reynolds numbers, the boundary layer is characterized by well-organized flow, which develops in fluid filaments of different velocities placed on each other, with viscous stresses appearing between them. The shear stress, which originates skin friction, can then be described by Newton's law for viscosity:

$$\tau = \mu \frac{\partial U}{\partial y} \longrightarrow \tau_w = \mu \left. \frac{\partial U}{\partial y} \right|_w$$

- **Turbulent boundary layer:**
  At higher Reynolds numbers, on the other hand, the flow is characterized by chaotic and multiscale flow. With respect to laminar flow, the turbulent boundary layer is characterized by an additional interaction consisting in the momentum transfer from different fluid filaments due to the turbulent velocity fluctuations, which adds up to the viscous stresses to make up the skin friction. The shear stress for the turbulent boundary layer can then be defined, according to the Reynolds decomposition, as:

$$\tau = \mu \frac{\partial U}{\partial y} - \rho \overline{u'v'}$$

  Where u' and v' are the components of the velocity fluctuations in the streamwise and normal to the flow directions, respectively. The term $-\rho\overline{u'v'}$ represents an apparent shear stress for the mean velocity and is

referred to as the Reynolds stresses; its value is positive if the amount of fluid moving towards the wall, characterized by negative v' component, carry an excess of momentum [20].

Since most engineering applications are characterized by higher Reynolds numbers compared to the values associated with laminar flow, the study of the phenomena which regulate the production of skin friction in turbulent boundary layers becomes increasingly important for developing effective drag reduction techniques.

1.1.1 Classical theory of the turbulent boundary layer

Unlike the laminar boundary layer, the turbulence boundary layer does not show a full similarity of the mean velocity profile [16], but is studied by dividing it into two regions: the inner layer and the outer layer. In the inner layer, the turbulent boundary layer mean velocity profiles are usually treated as proposed by Prandtl [21]. The mean streamwise velocity U and the wall distance y get scaled using two scaling parameters: the friction velocity, defined as $u_\tau = \sqrt{u/\tau_w}$, which scales the velocity, and the viscous length, defined as $l_\tau = \nu/u_\tau$, which scales the wall distance. Two non-dimensional quantities, referred to as wall units, are then defined:

- $u^+ = U/u_\tau$
- $y^+ = y/l_\tau$

When described by the non-dimensional wall units, the inner layer is found to follow an universal law, known as the wall of the law:

$$\frac{U}{u_\tau} = f(y^+)$$

The outer layer, on the other hand, is described by using δ, a measure of the boundary layer's thickness, as the length scale. The wall distance is then normalized as $\eta = y/\delta$. The outer region then follows an universal function, the wake function, which, however is not independent from the Reynolds number:

$$\frac{U}{u_\tau} = f\left(\eta, Re\right)$$

The wall law is mathematically defined by further dividing the inner layer in three sub-layers:

- **Viscous sublayer:**
  The layer closest to the wall, in which viscosity is dominant, is known as

the viscous sub-layer and is defined for $y^+ \lesssim 5$. In the viscous sub-layer, wall units follow a linear relationship:

$$u^+ = y^+$$

- **Logharitmic layer:**
  The outer region of the inner layer, defined for $30 \lesssim y^+ \lesssim 150$, the non-dimensional velocity follows a logarithmic profile:

  $$u^+ = \frac{1}{k} log(y^+) + B$$

  Where k is the Von-Karman constant and B is an intercept constant. This region is called the logarithmic layer, or, alternatively, the overlap region, because the description given by the wall law and the wake law should collapse for $y^+ \to \infty$ and $\eta \to 0$ at large Reynolds numbers [2]. The upper limit of the logarithmic region dependent on the Reynolds number, and can range from $y^+ = 80$ to the conventional value of $y^+ = 150$ [18].

- **Buffer layer:**
  The region between the viscous sub-layer and the logarithmic layer, in which the wall units transition from the linear profile to the logarithmic profile, is called the buffer layer.

In the viscous sub-layer, viscosity fundamentally accounts for all of the shear stress, while in the logarithmic layer viscosity is negligible and the Reynolds stresses become dominant. In the buffer layer, both viscous stresses and Reynolds stresses are important and turbulence reaches its peak production and dissipation.

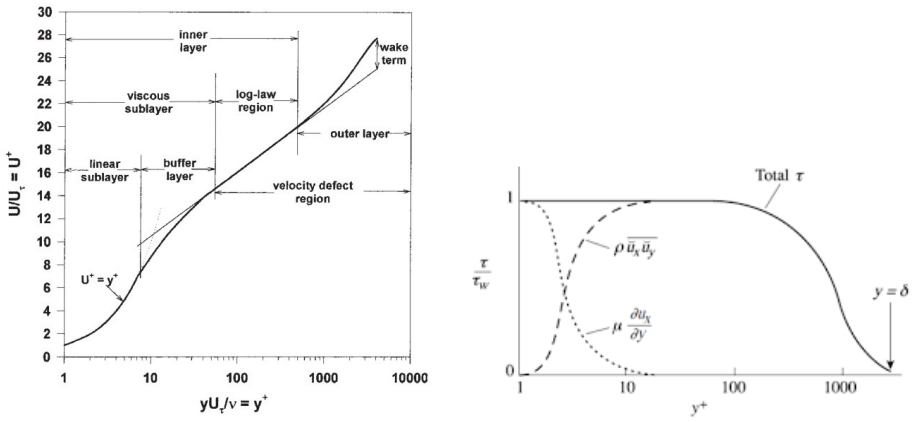

(a) (b)

Figure 1.2: (a) Turbulent boundary layer non-dimensional mean velocity profile, (b) evolution of the share of skin friction due to viscous stresses and to turbulent stresses with y^+

1.1.2 Near wall turbulent structures

The structure of the near wall mean streamwise velocity profile, which was described in the previous paragraph, is actually connected with the existence of coherent structures of turbulent nature, associated with velocity fluctuations around the mean velocity value. Those structures and their dynamics have been subject of intensive study, leading to a classification supported by a general consensus [30].

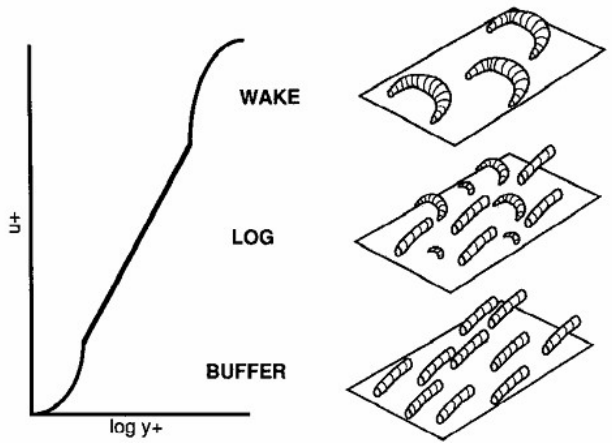

Figure 1.3: Schematic of the coherent structure populations in different regions of the turbulent boundary layer. Reproduced from [31]

The buffer layer is populated by low speed streamwise streaks and quasi-streamwise vortices as can be observed in the flow visualization reported in 1.4. Streamwise streaks are elongated and sinuous structures characterized by an alternatively negative or positive value of the streamwise velocity fluctuation u' spaced, on average, of $z^+ \approx 100$. Quasi-streamwise vortices are swirling structures whose axis, which is nearly aligned to the flow direction, has a slight upward tilt that increases with the distance from the wall [18]. This two types of structures are generated by a self-sustaining cycle, as the vortices result from the instability of the streaks and the low speed streaks are formed by low speed flow lifted from the region near to the wall by the streamwise vortices[15].

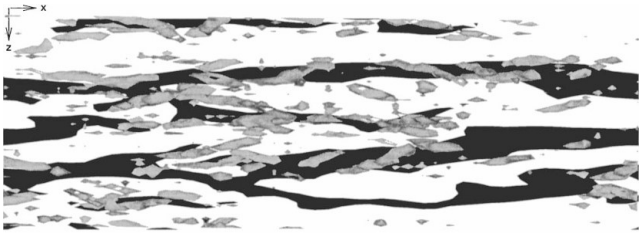

Figure 1.4: Visualization of the low speed streaks (black) and of the streamwise vortices (gray) at $y^+ = 20$. Reproduced from [32]

The streamwise streaks contain most of the flow's kinetic energy and are main contributors in the momentum transfer and in the generation of turbulence drag, while the upwash and downwash effect induced by individual quasi-streamwise vortices is also responsible for the production of tangential Reynolds stresses [20]. Above the buffer layer, the flow structure becomes more complex, as the multi-scale nature of turbulent motion gets more significant: the streamwise velocity is organized in much larger streaks and hairpin vortices, developed from the near wall structures, are found in packets [14].

1.2 Flow control methods for drag reduction

In aeronautic applications, such as commercial aircraft, skin friction drag accounts for approximately 50% of the total drag, hence making the development of skin friction reduction methods a promising approach to reducing fuel consumption, pollutant emissions and operating costs. The several methods that have been explored can essentially be subdivided into two classes:

- **Passive methods:**
  Flow control systems that do not require any sort of power supply
- **Active methods:**
  Drag reduction methods that rely on a dedicated power supply, although allowing for significantly larger values of drag reduction. Some of the most efficient active solutions are based on the spanwise oscillation of the wall or on the forcing of the flow actuated by jets.

1.2.1 Riblets

Among the passive flow control methods, one that has shown promising results consists in the permanent manipulation of the wall using micro-grooves generally referred to as riblets. This solution is already in use by some passenger airlines and has also found application in sports, such as sailing competitions and rowing events. It has been found that Riblets can reduce skin friction up to

10% in canonical flat plate flows, though lower performance is to be expected for more complex geometries. Flight tests carried out on an aircraft with 70% of its surface covered with riblets gave a 2% reduction in fuel consumption as a result [17]. Although fuel savings are achieved, cost savings may not be significant when we account for installation and maintenance costs. Therefore, in order to increase riblets performance, many studies focus on obtaining a deeper understanding of their flow physics.
The basic geometric configuration of riblet systems is the following:

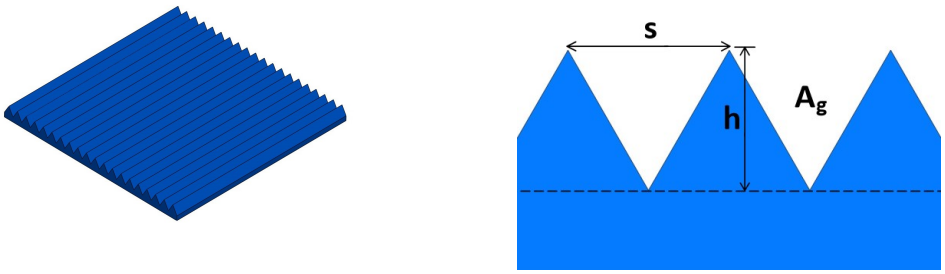

(a) (b)

Figure 1.5: A surface fitted with riblets (a), characteristic dimensions of riblets (b)

The depth of the riblets, h, and their spacing, s, represent two characteristic lengths for the riblets geometry definition.
The drag reduction mechanism, as it can be imagined, is related to the Reynolds number; Walsh & Lindemann [22] showed that this dependence could be highlighted by expressing riblet dimensions in wall units:

$$L^+ = \frac{Lu_\tau}{\nu}$$

Where L is the considered characteristic length.
The groove spacing, s, is a commonly used measure for the riblet characteristic length L, although Garcia-Mayoral & Jimenez [10] have found a different dimension l_g, defined as the square root of the groove cross section, $\sqrt{A_g}$, which takes into account the groove shape.
Different drag reduction regimes can be seen when representing diagrams showing the normalized variation of skin friction with respect to the smooth wall case ($\Delta\tau/\tau_0$), where τ_0 is the wall shear stress for the smooth plate case, as a function of the riblet dimensions expressed in wall units.

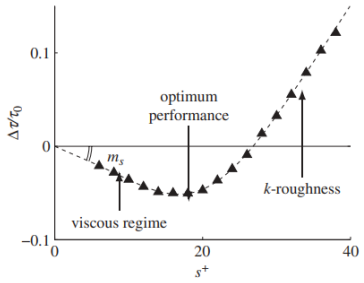

Figure 1.6: Drag-reduction regimes observed over triangular riblets with 60° tip angle, as a function of the spacing s^+, reproduced from [10]

The first portion of the drag reduction curve shows a progressive decrease in drag, until reaching a minima for $s^+ \simeq 15$. This is called the viscous regime. Subsequently to the viscous regime breakdown, drag increases, adopting the typical roughness behavior.

The drag reduction mechanism

The drag reduction mechanism in the viscous regime is still under discussion to this day. Bechert *et.al* [5] has attributed it to the inhibition of the spanwise movement of the near wall streamwise vortices, while a different and more recent interpretation has been given by Choi *et.al* [11], Suzuki & Kasagi [33] and Goldstein [4], who found that riblets reduce drag by shifting the streamwise vortices further away from the wall, thus reducing turbulent mixing near the wall and, hence, skin friction.

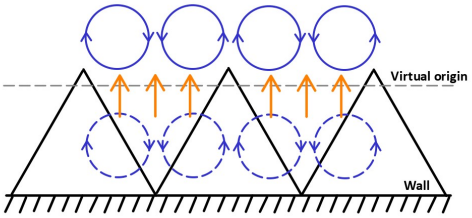

Figure 1.7: Schematic representation of the upward lift of the streamwise vortices

A quantitative idea is that wall surfaces with applied riblets are seen by the turbulent flow as an equivalent smooth wall placed at a virtual origin, Δ_u being the virtual origin position for the streamwise flow and Δ_w that of the spanwise flow. Near the wall, the flow behaves as a uniform shear, thus following a linear profile:

$$u \propto y - \Delta_u$$
$$v \propto y - \Delta_v$$

Luchini [27] has noted that the offset between this two heights, the "protrusion height", defined as $\Delta h = \Delta_v - \Delta_u$, is related to drag reduction: if the virtual origin of the spanwise flow is displaced further from the wall than the virtual origin of the streamwise flow (*i.e.* $\Delta h > 0$), then the lateral motion induced by the streamwise vortices is impeded with respect to the smooth wall case. The vortices have been lifted away from the wall and therefore the turbulent mixing of the streamwise momentum, which is responsible of the near wall shear forces, is reduced [10].

The role of riblets shape

Riblets can be built in different shapes, which result in different geometries of the resulting grooves. Garcia-Mayoral & Jimenez [10] have found a characteristic dimension l_g, defined as the square root of the groove cross section, $\sqrt{A_g}$, which takes into account the groove shape and allows good data collapsing for the drag reduction diagram.

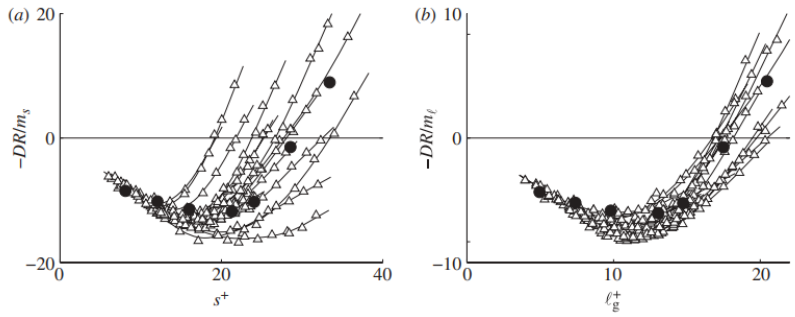

Figure 1.8: Drag reduction diagram as a function of the riblets spacing (a) and of the square root of the cross-sectional groove area (b). Open triangles, experimental results, filled circles, DNS data. Reproduced from [10]

The collapsing of the data in figure 1.8 shows that the location of the viscous regime and of the maximum performance are independent of the riblets shape, although the drag reduction obtained itself depends on the groove geometry. A general result is that sharper riblets provide greater drag reduction in the viscous regime, while the different shape does not lead to a different behavior in the drag increasing regime. This trend can also be observed when studying the effect of wear on riblet performance: tip rounding caused by erosion affects the system's drag-reducing capabilities.

1.2.2 Sinusoidal riblets

One of the latest advancements in the study of riblets tackles the implementation of unconventionally shaped riblets whose crests do not develop in a

straight line but following a sinusoidal pattern. These riblets are referred to as sinusoidal riblets, or, often, as wavy riblets.

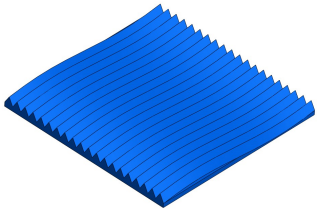

Figure 1.9: A surface fitted with sinusoidal riblets

Cafiero & Iuso [8] obtained an additional 3% of drag reduction when using sinusoidal riblets instead of longitudinal riblets at a friction Reynolds number of nearly 1200. It was found [9] that in the drag reducing regimes sinusoidal riblets yield narrower and more closely spaced low speed streaks in the near wall region, with respect to longitudinal riblets. This has been attributed to the fragmentation of the turbulent structures due to the periodic transversal flow induced by the curved grooves. The turbulent structures are thus weakened by the fragmentation process, resulting in lower turbulence production and Reynolds stresses. This mechanism resembles, in some way, that of the oscillating wall active method, making the sinusoidal riblets effects on drag reduction a combination of those of conventional longitudinal riblets and that of the aforementioned active drag reduction method.

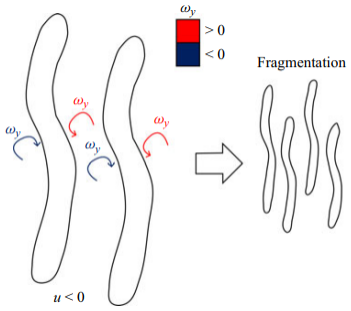

Figure 1.10: Schematic representation of the low speed streaks fragmentation due to the sinusoidal riblets. Reproduced from [9]

1.3 Aim of this work

Given the growing importance of developing drag reduction systems aimed at reducing costs and emissions in the aerospace sector, the study of riblets has become a recurring topic in academic research. For this reason, wind tunnels for boundary layer observations have become essential instruments for academic research laboratories. Politecnico di Torino has itself become a point of reference on riblets research and, more in general, in the study of flow control methods. To continue research in this field and further expand the knowledge of the physics of drag reduction mechanisms, the fluid-dynamics research group of the Politecnico has undertaken a renovation of the pre-existing experimental facility. In this work, the last steps of the new wind tunnel assembly as well as the design and implementation of some new solutions for the improvement of the experimental set up will be covered. Then, the fluid-dynamic characterization of the new facility will be carried out and, finally, some observations on riblet manipulated flows will be conducted, comparing the results with previous works.

1.3.1 Previous works conducted at the Politecnico di Torino laboratory

Many studies on flat plate flows and flow control systems have already been conducted in the Modesto Panetti laboratory of the Politecnico di Torino, leading to interesting findings. In 2022 Cafiero and Iuso [8] conducted the first observations on sinusoidal riblets, testing two wavy riblets configurations with a fixed wavelength and two different values of the amplitude. The investigated sinusoidal riblets have been compared with conventional longitudinal riblets and with an equivalent smooth plate.

	RLONG	RS1	RS2
$s\ [mm]$	0.30	0.30	0.30
$h\ [mm]$	0.21	0.21	0.21
h/s	0.70	0.70	0.70
$a\ [mm]$	0	0.15	0.60
$\lambda\ [mm]$	∞	19.2	19.2
N_λ	n.a.	13	13

Table 1.1: Geometric data of the riblet configurations tested in [8]

By carrying out force measurement on floating testing plates, they found out that wavy riblets generally yield higher values of drag reduction, obtaining values as large as 10%.

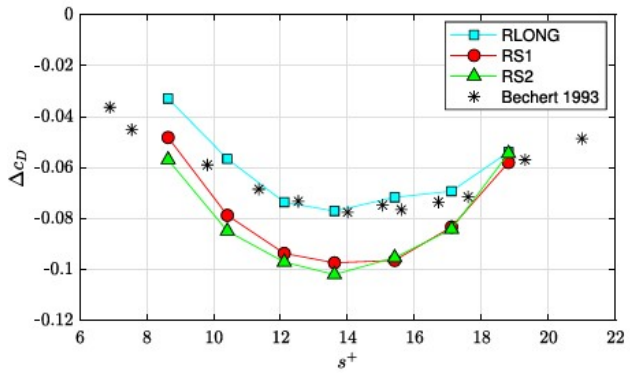

Figure 1.11: Drag reduction curve the riblet configurations tested in [8]. Reproduced from [8]

Hot wire anemometry measurements as well as particle image velocimetry (PIV) visualizations have been used to statistically prove that the sinusoidal riblets are responsible for an attenuation of the Reynolds shear stresses and, thus, of the turbulent drag. They then showed, through the detection of accelerated events in the buffer layer, that sinusoidal riblets lead to the weakening of the intensity of the turbulent structures in the streamwise plane, while enhancing the spanwise induced motion.
In 2024, sinusoidal riblets have been further studied by Cafiero, Iuso and Amico [9]. New PIV experiments were conducted to investigate the effect of sinusoidal riblets on the near wall organization of the coherent structures responsible of the skin friction production. The investigation has involved the identification of the topology of the low speed streaks by using conditional average techniques. The idea that sinusoidal riblets induced the weakening of the streaks was confirmed, and the high values of the wall normal vorticity found at the streak edges suggested the idea that the fragmentation is due to the spanwise motion induced by the curved path imposed by the sinusidal riblets.

1.3.2 The old facility configuration

The facility used to carry out the mentioned works consisted of a low speed, open-circuit, wind tunnel, belonging to the Modesto Panetti laboratory of the Politecnico di Torino.
The wind tunnel had a 3999 mm long testing chamber with rectangular section, preceded by a settling chamber fitted with a honeycomb and mesh screens for large-scale turbulence breakdown and a contraction with a 9:1 area ratio. The test section height is fixed at 510 mm, while the width spaces from 699 mm to 768 mm, as the vertical walls are slightly divergent, with an angle of 0.5°. This slight expansion of the testing chamber section is intended to limit the speed increasing effect due to the flow passing section contraction

Figure 1.12: The old wind tunnel configuration in the Modesto Panetti laboratory

resulting from the boundary layer thickness development on the walls.
The test section ended with an "L" shaped duct, which used to deflect the flow upwards to avoid interference with a nearby wind tunnel; the duct was fitted with aerodynamic fins to guide the flow and prevent separation.
The boundary layer observations were conducted on a flat plate located at the 50% of the test section height, resulting in the halving of the transverse section; this area reduction was obtained by a contoured transition achieved with a smooth connection between the test section floor and the top surface of the flat plate, which also served to insulate the measuring equipment below the flat plate from the flow. This solution implied the conception of a boundary layer suction system to inhibit the growth of the wind tunnel wall's boundary layer on the flat plate.

1.3.3 The facility's reconfiguration project

The described facility has recently been subject to a renovation project, which has been covered in [29].
The new project has included:

- The lengthening of the wind tunnel straight segment
- Replacement of the terminal "L" shaped duct with a truncated pyramid-shaped duct
- A new flat plate design
- The repositioning of the measuring station

Figure 1.13 shows the CAD model of the newly projected wind tunnel. The three central sections of the testing chamber represent the old configuration

tunnel. The two 500 mm sections added at the two ends extended the test section length from 3999 mm to 4999 mm, allowing the installation of a longer flat plate. The terminal truncated pyramid-shaped divergent has a length of 1500 mm and an area expansion ratio of 2.04.

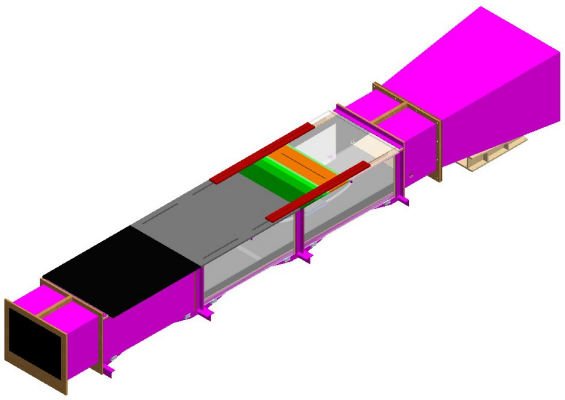

(a)

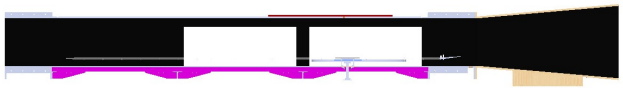

(b)

Figure 1.13: CAD of the new wind tunnel design in axonometric view (a) and lateral section view (b)

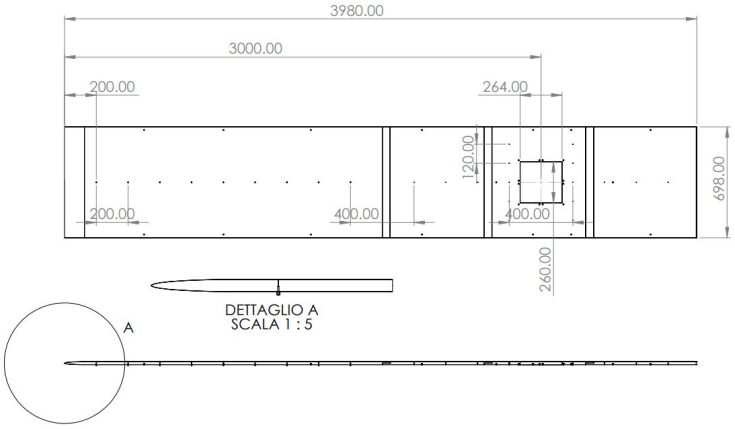

Figure 1.14: The new flat plate design, with detail of the elliptical leading edge

In figure 1.14 the drawing of the new flat plate is shown. The plate is fitted with an elliptical leading edge, 29 pressure taps lodgings and a hollow slot that will accommodate the different tested plates. The pressure taps are divided into 17 longitudinally arranged probes, aligned with the main axis of the flat plate and equally spaced, and 12 transverse probes, positioned upstream and downstream to the measuring station.
At the rear end of the flat plate, an adjustable flap will be installed and used to guarantee the zero pressure gradient conditions on the plate.

1.3.4 Objectives

To realize the aim of this work, the following objectives have been outlined:

- Free-stream flow characterization on the tunnel section
- Acquisition of the pressure field on the flat plate
- Evaluation of the effect of the flap on the pressure distribution
- Study of the behavior of the turbulent boundary layer along the flat plate
- Boundary layer acquisition on riblets

The first four objectives, which relate to the facility characterization, will be presented in chapter 3, while the riblet manipulated boundary layer observations will be covered in chapter 4.

Chapter 2

Experimental setup

The architecture of the experimental facility subjected to the renovations has been already illustrated in 1.3.3. At the beginning of the activities, the new top and side panels of the tunnel and the terminal divergent duct had already been installed and the remaining operations to carry out to complete the setup were the installation of the flat plate and the arrangement of the measuring systems.

2.1 Flat plate installation

The new flat plate for the boundary layer observations is fabricated in plexiglass and is formed by two sections of equal length that had to be mounted together. Six wooden slats, two of which spanning across the two different plate sections, fitted with height-adjustable legs, have then been mounted on the lower face of the plate. Another feature of the plate is the presence of 29 fitting holes for the realization of static pressure probes; the small holes have been provided with steel inserts and connected to the pneumatic lines. The flat plate assembly has then been positioned in the testing chamber of the wind tunnel. The legs of the plate supports were adjusted to make the plate perfectly horizontal and the gaps between the diverging lateral walls of the wind tunnel and the plate edges have been sealed using polystyrene shaped spacers, to avoid aerodynamic effects due to the differential pressure between the flow over and under the plate.

2.1.1 Design and installation of the flap

An important requirement for boundary layer observations is that the flat plate flow characteristics are met: the flow should experience a near zero pressure gradient along the plate length and the stagnation point should be centered on the leading edge. This is not straightforward when long flat plates are

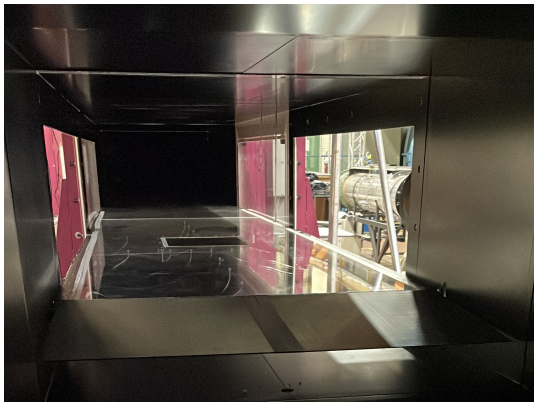

Figure 2.1: The flat plate installed in the wind tunnel

employed and the wind tunnel cross-section is relatively small when compared to the plate dimensions. The growth of the boundary layer on both the flat plate and the wind tunnel's top and lateral walls, in fact, normally results in a "virtual" area contraction along the flow direction, which induces a negative pressure gradient over the test section length. A common solution to compensate for this negative pressure gradient is using diverging walls, but the compensating effect produced is optimal for a specific operating condition if the divergence angle is fixed. A typical method to extend the field of the realizable zero pressure gradient operating conditions is to use a flapping surface at the back of the plate to induce a positive pressure gradient and compensate for the existing negative pressure gradient. To overcome the necessity of optimizing the pressure gradient compensation, a flap with 350 mm chord length, 20 mm maximum thickness and 700 mm span was designed. The flap has been manufactured in two 3D printed PLA half-span parts that have been mounted together with the with the interlocking of three connecting pins. Two screws, fastened on each of the two flap edges, will serve to fix the rotation axis and adjust the deflection angle. The flap will be mounted and adjusted through custom-designed 3D printed connection elements that will be fixed in the two slots present on each side of the wind tunnel lateral walls. In the first of the two slots the rotation axis will be fixed by a tight hole, while in the second slot the deflection angle will be regulated by adding different combinations of spacers to the support plane of the second screw of the flap.
Two sets of dedicated spacers have been manufactured, allowing the realization of the deflection angles in table 2.1.

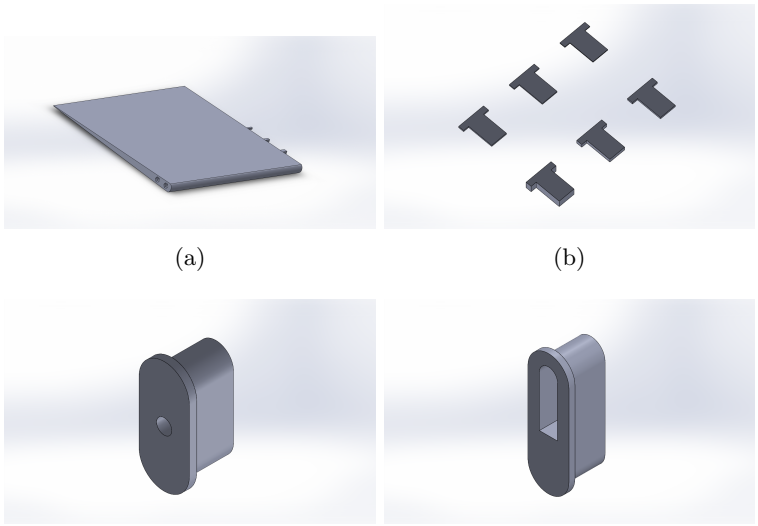

(a) (b)

(c) (d)

Figure 2.2: (a) Half-span section of the flap, (b) set of spacers for angle adjustment, (c) rotation axis hinge, (d) spacer-adjustable support surface for angle adjustment

s	α
4.4 mm	0°
4.8 mm	1°
5.2 mm	2°
5.6 mm	3°
6 mm	4°
6.4 mm	5°
6.8 mm	6°
7.2 mm	7°
7.6 mm	8°

Table 2.1: Realizable flap incidence angles with relative total height of the necessary spacers

2.1.2 Turbulence tripping devices

Turbulence tripping devices consist of small structures that can be used to perturb naturally laminar boundary layers, triggering the transition to a turbulent boundary layer. Two different types of turbulence tripping structures will be tested. The first trip type is a sawtooth fence, a paper strip with triangular shaped obstacles on both sides. The triangular obstacles will be kept bent in the horizontal position. In this way, the flow will not be strongly perturbed and the generated turbulent boundary layers will be characterized by moderate momentum thickness Reynolds numbers Re_θ. This trip will be referred to as

"sawtooth". The second trip type, which will be referred to as *"2row20"*, consists of two rows of cylinders of the same geometrical characteristics of those used in [7] and will, conversely, serve to generate high Re_θ turbulent boundary layers. However, this type of tripping device strongly disturb the flow, and the resulting turbulent boundary layers could exhibit an altered structure; The canonical characteristics of the flow may then be recovered only after a certain "adaptation region".
Turbulence tripping devices can generally be divided into two categories [25]:

- **Wall driven:**
  Turbulence tripping mechanisms with shorter adaptation region and little interaction between the inner and outer boundary layer regions. They result, however, in a more perturbed outer part of the boundary layer, with respect to wake driven mechanisms. Typical wall driven trips consist of small cylinders with vertical axis.

- **Wake driven:**
  Turbulence tripping mechanisms with a typically longer adaptation region, where the interaction between the inner and outer part of the boundary layer is stronger, resulting in an altered inner structure of the boundary layer.

The 2row20 trip falls into the category of the wake driven trip devices for the artificial generation of high Reynolds number boundary layers. Following the work done by Rodríguez-López, Bruce and Buxton [7], the two different types of turbulence tripping structures will be tested, to compare their performance and influence on the boundary layer structure. Both the tripping devices have been alternatively fixed on the flat plate with paper tape at $x \simeq 0.2\ m$ from the leading edge.

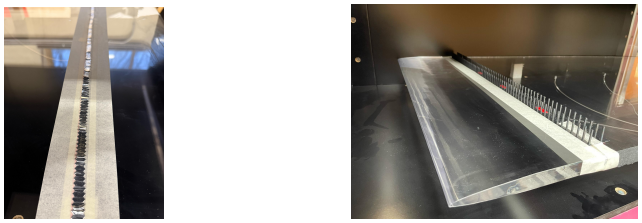

(a) (b)

Figure 2.3: (a) sawtooth trip, (b) 2row20 trip

2.2 Measuring systems

Many measuring techniques have been historically employed to study the performance of riblets and their effect on the boundary layer structure. The in-

fluence of the riblets on the boundary layer flow is typically studied by means of hot wire anemometry when it is sufficient to measure the 1D mean velocity profiles and the flow statistics connected with the streamwise flow in the near wall region and compare them with the ones of turbulent boundary layers developed on a smooth plate. Conversely, PIV techniques are used when the topology of the near wall turbulent structures needs to be studied. Riblet performance, on the other hand, is commonly assessed by means of integral force measurement on riblet equipped tiles, using load cells or LVDT based displacement measuring systems.
To fulfill the purpose of this work, the technique that will be mainly used is the hot wire anemometry, but pneumatic measurement systems will also be involved for the hot wire calibration and the pressure field characterization.

2.2.1 Pressure measurement systems

Pressure measurements will be carried out to obtain the flow velocity in the wind tunnel through a Pitot-type probe, as well as to study the pressure distribution along the flat plate through the pressure taps installed on the flat plate. Two different manometers will be used to perform the acquisitions:

- **Furness Controls FCO560 precision manometer:**
  The FCO560 is a portable differential manometer with 0.01 Pa precision and 10 Hz acquisition frequency. It has been used to measure the dynamic pressures from the Pitot tube positioned in the wind tunnel and, thanks to its high precision, allowed the hot wire probe calibration. The FCO560 readings have been collected via serial communication during the execution of the acquisitions.

Figure 2.4

- **Scanivalve ZOC 33/64px:**
  The Scanivalve ZOC 33/64px is a 64 channels electronic pressure scanner which employs piezoresistive sensors to measure differential pressure with environmental pressure as reference value.

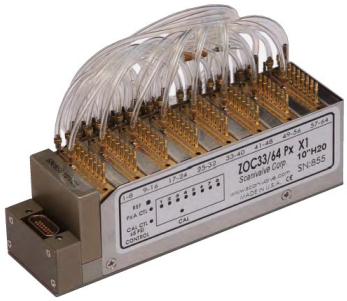

Figure 2.5

2.2.2 Hot wire anemometry

The hot wire anemometry is one of the most used techniques to obtain measurements in turbulent flows. Its main advantages with respect to pneumatic measurement systems are its high sampling rates, which allow to capture the high frequency velocity fluctuations connected to the small-scale turbulent structures, and its low interference with the flow, due to its reduced dimensions.
Typical hot wire systems for fluid dynamic measurements rely on "constant-temperature anemometry" (CTA): a thin, electrically heated wire, whose resistance varies with temperature, is placed in the flow and is subjected to forced convection. As the fluid velocity cools the wire, the electric current supplied to the circuit is varied by a servo-amplifier to maintain its temperature at a constant value. The voltage needed to balance the wire cooling is then related to the flow velocity performing the calibration of the system. One drawback of this technique is, therefore, the need of calibrating the system, whose calibration curves are also quite sensitive to ambient conditions.
The hot wire anemometry system arranged in the experimental setup involved in this work includes:

- **Dantec P15 hot wire probe:**
  Hot wire sensor dedicated to boundary layer acquisitions, which features bent downward supports that facilitate near wall measurements.

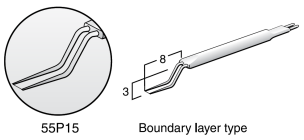

Figure 2.6

- **Dantec Streamline Pro anemometer:**
  The anemometer contains the Wheatstone bridge circuit on which the CTA anemometry is based. This specific system allows to automatically balance the Wheatstone bridge in the dedicated Streamware Pro software.

Figure 2.7

- **National Instruments NI9215 module:**
  Analog input module which allows the conversion of the electric signals emitted by the anemometer

Hot wire calibration

The hot wire probe has been periodically calibrated *in situ*, using the Pitot tube's dynamic pressure measurements to determine the reference velocities that have been correlated to the hot wire readings. Firstly, the hot wire's offset tension, that is the potential difference experimented by the Wheatstone's bridge when the probe is not subjected to forced convection, has been measured; then, the wind tunnel's operating regime has been varied and both the velocity of the flow and the hot wire electric output have been measured, through, respectively, the Pitot's tube and the hot wire probe at the different flow speeds. 4th grade polynomials have been used to obtain the calibration curves for the hot wire probes.

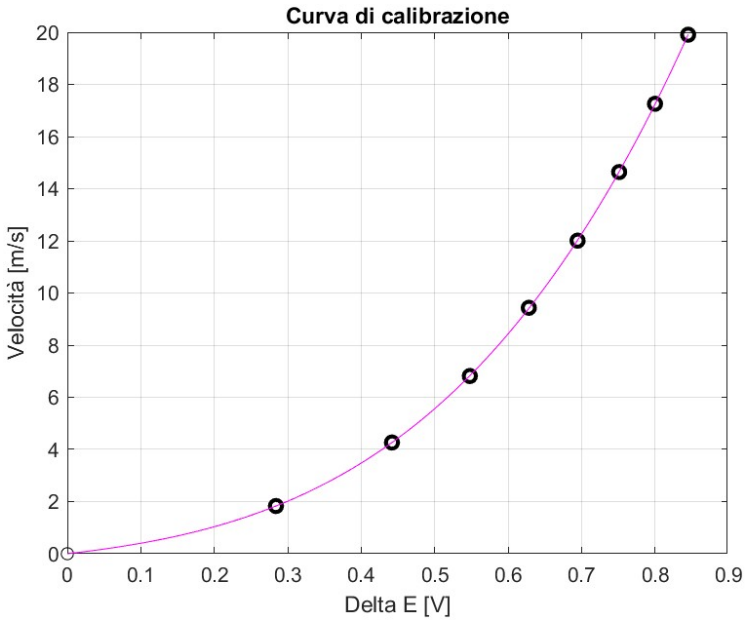

Figure 2.8: Example of calibration curve assessment

2.3 Probe positioning systems

A key requirement to carry out the flow characterization and boundary layer acquisitions is the translation of the probes in the z (*spanwise*) and, even more critically, in the y (*wall normal*) directions. To do so, a bi-directional motion system was prepared, employing two different types of linear stages:

- **Zaber motion x-lsm series linear stage:**
  Linear stage with a maximum travel of 203.2 mm and an accuracy of 60 μm. It was implemented to manage the vertical movement of the probes, which need high resolution to carry out boundary layer acquisitions. The pitot tube and the hot wire probe support were fixed to this linear stage's kart with an appropriate probe holder.

- **Stepper motor driven SKF linear guide:**
  A longer linear guide, driven by a stepper motor, was employed to operate the horizontal movement of the measuring systems. The linear guide features a maximum travel of 470 mm and a pitch of 5 mm.

The vertical linear stage was arranged on the horizontal linear stage kart to constitute the bi-directional probe positioning system.

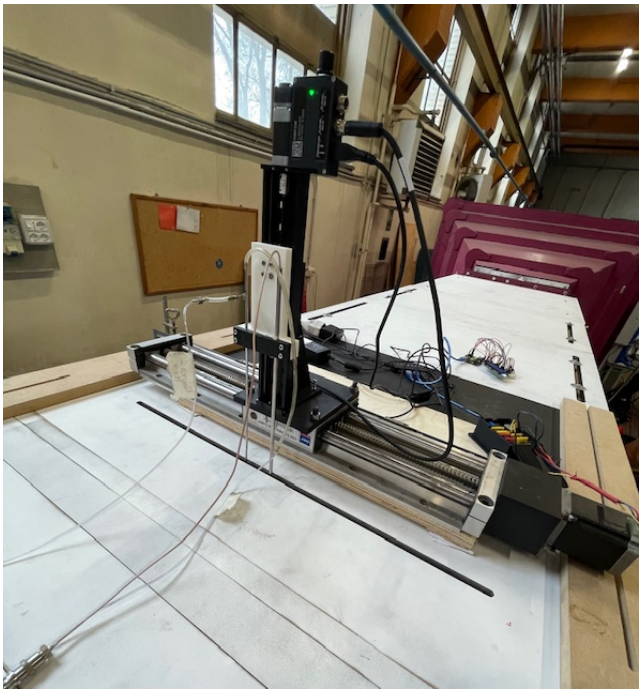

Figure 2.9: Probe positioning system

To vary the x (streamwise) measuring position, the entire assembly was physically moved and the wind tunnel's top panels were appropriately swapped to position the panel with the probe slot in the desired location.

2.4 Riblet testing station setup

The riblet manipulated boundary layer observations will be conducted on 258 x 258 mm riblet equipped tiles accommodated in a 264 x 260 mm hole realized on the flat plate. The gap between the testing plates and the surrounding flat plate will serve to allow the plate to float, enabling future force measurements via LVDT displacement sensors. The flow will then transit from a smooth region to a riblet manipulated surface, passing over a few millimeters wide gap. These two issues entail the need of dedicated systems to ensure that the boundary layer behaves correctly over the testing plate.

2.4.1 Testing plate alignment system

One of the requirements of the riblet testing setup is that the floating plate is correctly aligned to the surrounding flat plate. To manage the adjustment of the height and tilt around the x (*streamwise*) and z (*spanwise*) axes, a dedicated system was designed. This system has been conceived to be compatible

with the LVDT sensors-based system for force measurements, which, however, will not be employed in this work. The vertical displacement of the plate will be carried out using a Thorlabs manual jack whose two ends will be connected, respectively, to the overlying tilt control system and to a support base. The support base could either be a moving plate carried by linear guide's karts if the force measurement system is implemented or a fixed wooden plate.

Figure 2.10: Thorlabs jack

The tilt control system, which will be installed over the jack, will instead consist of a specifically designed articulated support. The main requirements that have been identified for this device are:

- The ease of actuation of the control and of the installation of the different plates
- The small entity of the lateral displacement of the plate consequent to its rotation
- The stiffness of the assembly

The designed device employs three micrometer screws to tilt the plate by adjusting its three contact points.

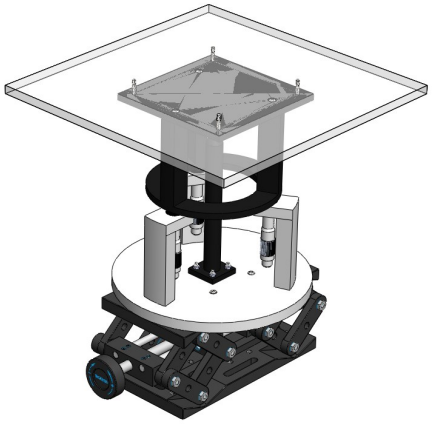

Figure 2.11: Height and tilt adjustment system for the test plates

The three micrometer screws are supported by three mounts connected to the system's base and act on the plate through a dedicated frame, connected to the testing plates by four M3 screws. This solution was chosen to facilitate the access to the screws, that will lay outside the wind tunnel's walls. The center of the plate has been fixed by a ball joint mounted on a vertical support. The housing of the ball joint has been realized on the plate support frame and features threaded external walls, while a threaded cap running on the vertical support allows for the tightening or loosening of the joint. This solution minimizes the lateral displacement of the plate during its rotation, and ensures a sufficient stiffness of the assembly. The ball joint locking system is intended to facilitate the substitution of the tested plate, as the plate can be removed while connected to the frame once the joint is unlocked.

2.4.2 Labyrinth seal and fairing

The other requirement of the setup is that the gap between the flat plate and the floating tile does not affect the boundary layer. To avoid this a 3d printed labyrinth seal, whose design was inspired by the one used in [23] was installed under the mentioned gap.

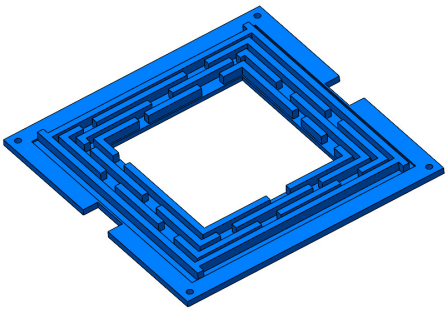

Figure 2.12: Custom designed labyrinth seal, inspired by the one used in [23]

A polyethylene fairing was then installed to insulate the testing plate supports and the passage hole in the wind tunnel floor from the airflow underneath the flat plate. The faring has been given a streamlined shape by passing the polyethylene sheets through custom-shaped supports screwed onto the flat plate's lower side.
An overview of the experimental setup for the hot wire boundary layer observations on the testing plates is reported in figure 2.13

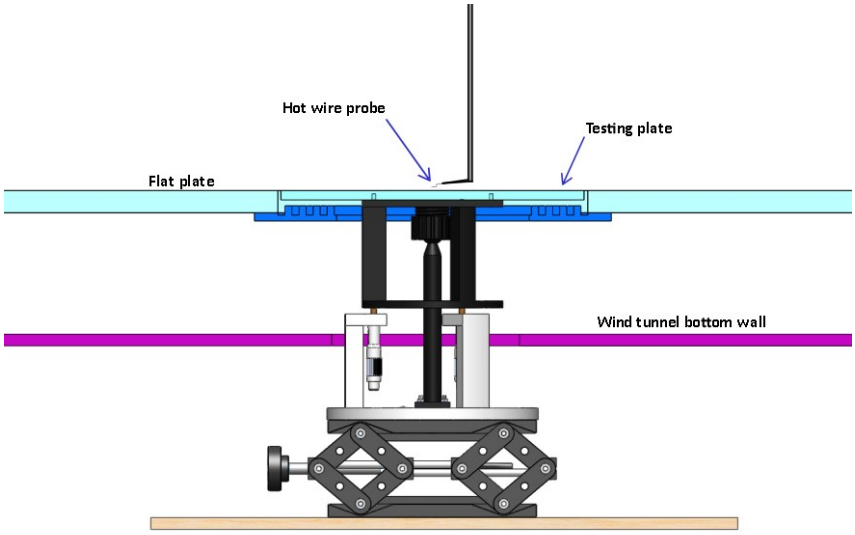

Figure 2.13: Overview of the setup of the testing station for the riblet manipulated boundary layer observations

Chapter 3

Experimental setup characterization

The preliminary characterization of the experimental setup, which constituted a substantial part of this work, will be described in depth in this chapter. Several activities were performed to evaluate the general flow quality as well as to ensure that the main requirements for conducting turbulence manipulation studies were satisfied. These are the satisfaction of the zero pressure gradient condition over the flat plate and the correct behavior of the boundary layer. Therefore, the experimental results that will be reported include pressure field observations through the flat plate's pressure taps, free stream flow acquisitions through hot wire anemometry and boundary layer acquisitions.

3.1 Flow characterization on the wind tunnel section

Free stream acquisitions have been taken in 5 different positions along the wind tunnel's test section ($x = 0.395\,m$, $x = 1.065\,m$, $x = 1.735\,m$, $x = 2.405\,m$, $x = 3.075\,m$) at the same inlet conditions. The acquisitions have been made on a $x - z$ measurement plane with $50\ mm \leq y \leq 200\ mm$ and $150\ mm \leq z \leq 150\ mm$, with $y = 0$ being on the surface of the flat plate and $z = 0$ being on the symmetry plane of the wind tunnel.

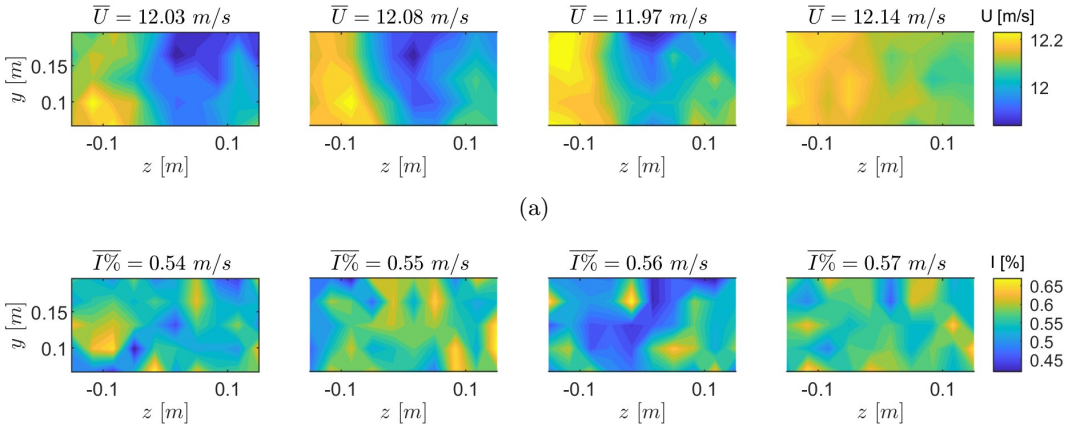

Figure 3.1: Evolution of the contour plots of (a) the velocity distribution, (b) the turbulence intensity level, on the tested transversal planes. The flow direction is from left to right

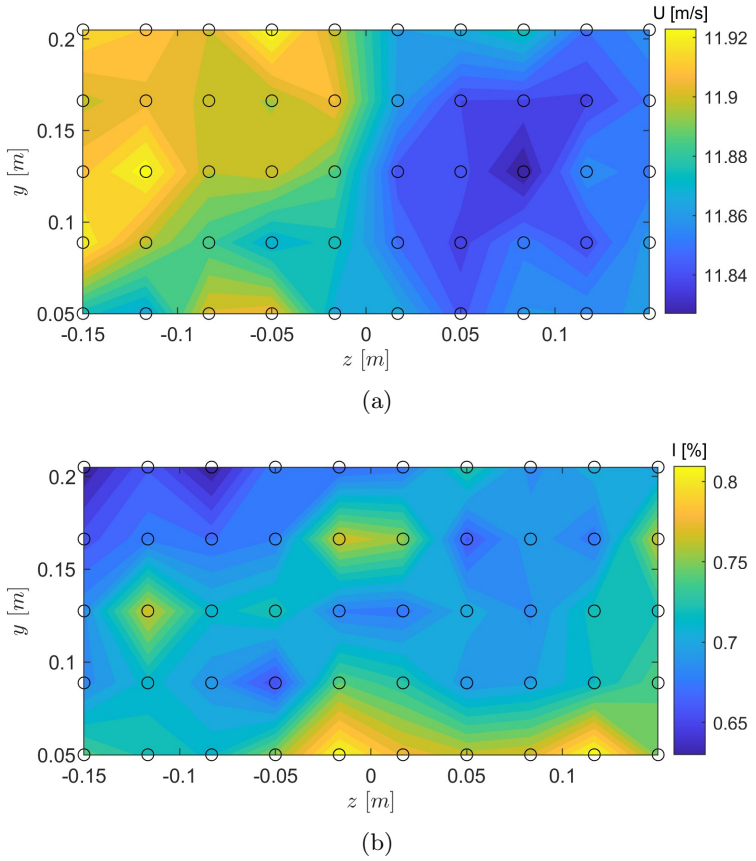

Figure 3.2: Contour plots of (a) the velocity distribution, (b) the turbulence intensity level above the riblets test station. The black circles represent the hot wire measurement points

The acquisitions at $x = 3.075\,m$, showed in figure 3.2a, that correspond to the measurement station for the riblet observations, show a slight asymmetry of the flow. The velocity variation on the acquisition section remains within $\pm 0.4\,\%$ at the tested flow velocity.
In figure 3.1a, the velocity distributions at the other measurement positions show a similar asymmetric pattern, suggesting that this asymmetry originates upstream of the test section inlet, possibly due to the fans of the wind tunnel engine system or within the settling chamber.
As shown in figure 3.1b, the mean turbulence intensity level remains constant at $\overline{I\%} \simeq 0.56$ across the first four measurement positions, but then increases to the value of $\overline{I\%} = 0.71$ in the transversal plane measured above the riblet testing station. This has been attributed to the boundary layer growth, which could, at a certain distance along the wind tunnel test section, influence the turbulence of the free-stream flow, making it impossible to get a "true" free-stream turbulence measurement. Regardless, the turbulence intensity level distributions do not show any specific pattern, but are characterized by a nearly constant value with some localized peaks, as expected.

3.2 Pressure distribution along the flat plate

Pressure field measurements have been conducted through the pressure taps installed on the flat plate to verify that the zero pressure gradient conditions were achieved with sufficient accuracy.

3.2.1 Natural pressure distribution

The pressure field was first observed before installing the flap. Figure 3.3 shows the differential pressure, with the ambient pressure as the reference value, measured by the pressure taps displaced along the flat plate. The flow velocity was set at $20 m/s$ for this test. The pressure distribution shows an initial slight increasing trend, possibly due to the effect of the wind tunnel diverging walls, followed by a strong decrease of the flow's static pressure, due to the effect of the boundary layer growth development.

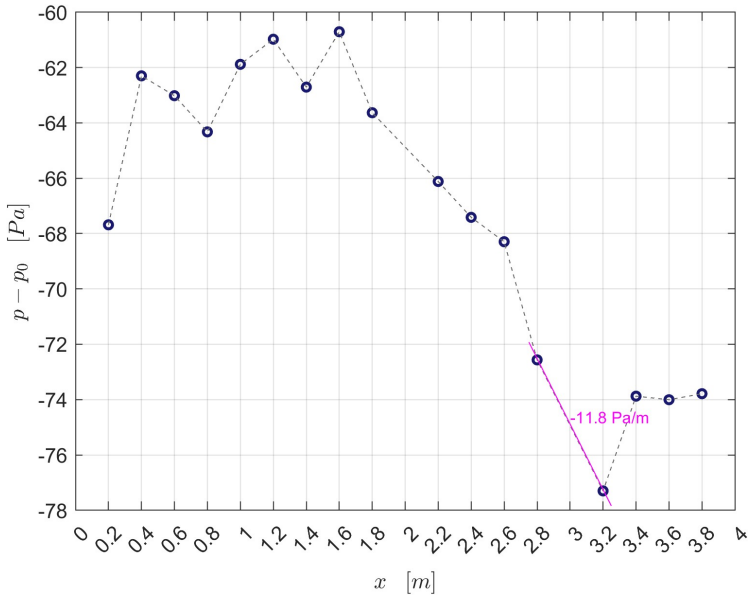

Figure 3.3: Differential pressure distribution, with ambient pressure p_0 as reference value. The flow velocity is set at 20 m/s and the flat plate's terminal flap installed.

The local pressure gradient above the riblets testing station, located at $x = 3\ m$ was evaluated by considering the difference between the measurements of the pressure taps upstream and downstream of it.

3.2.2 Effect of the flap

To study the effectiveness of the designed flap, pressure distribution observations have been made at different flow velocities and flap deflection angle values. Two parameters have been used to evaluate the flap effectiveness:

- Local dimensional pressure gradient above the riblet testing station
- Variation of the non-dimensional coefficient defined as $\tilde{c_p} = \frac{p-\bar{p}}{\frac{1}{2}\rho V^2}$

The local dimensional pressure gradient is related to the stability of the boundary layer over the riblet testing station, but its value can only be roughly estimated by the difference between the pressures measured by the probes immediately upstream and downstream to the plate. This criterion also only gives an information on the local characteristics of the boundary layer flow. The variation of the $\tilde{c_p}$ non-dimensional parameter, on the other hand, allows for a comprehensive evaluation of how well the zero pressure gradient conditions are reproduced along the flat plate, ensuring that the boundary layer develops correctly over it.

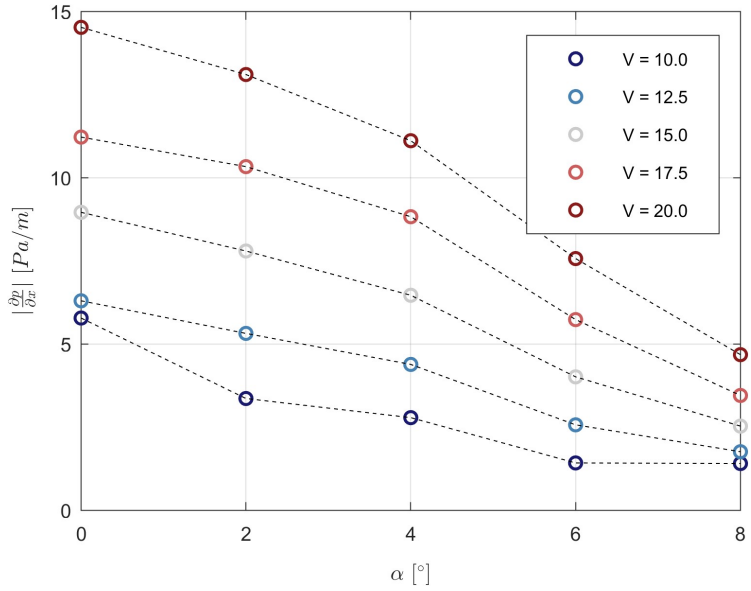

Figure 3.4: Estimated dimensional pressure gradient over the riblet testing station

In figure 3.4 the trend of the pressure gradient over the riblets testing station at different flow velocities is presented. It can be seen that for higher velocities the flap is more effective in reducing the pressure gradient, which is reduced by a factor of three by bringing the flap deflection angle from 0° to 8°

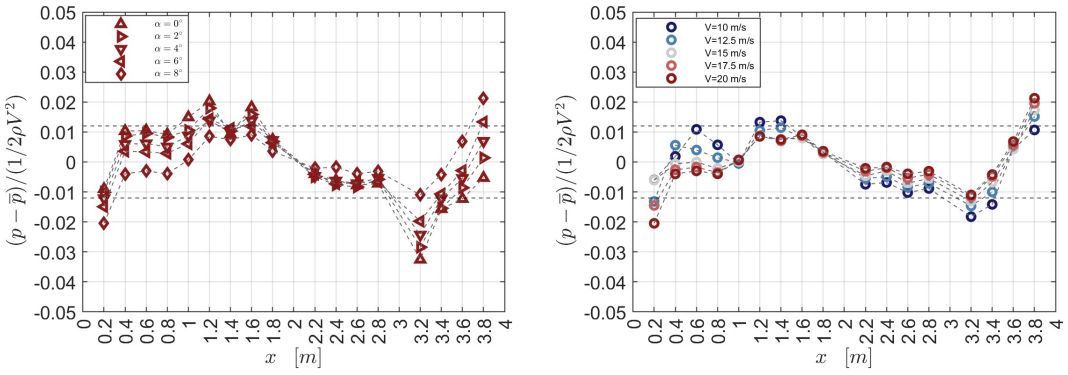

(a) (b)

Figure 3.5: Non-dimensional pressure distributions, (a) for different flap deflection angles α at $U = 20\ m/s$ flow velocity, (b) for different flow velocities at fixed flap deflection angle $\alpha = 8°$.

In figure 3.5a the non-dimensional pressure distributions at different flap deflection angles, relative to experiments at $U = 20\ m/s$ flow velocity, are shown together with dashed lines representing a $\tilde{c_p}$ variation of ± 0.012 as reference. The $\tilde{c_p}$ values for the higher tested flap angle $\alpha = 8°$, except for the first and

last probes, lie within -0.012 and 0.012. Similar values were considered as acceptable in [1] and [19]. In figure 3.5b the non-dimensional pressure distributions at the fixed value $\alpha = 8°$ of the flap deflection angle are shown for different flow velocities. It can be noted that, since the geometry is fixed, the $\tilde{c_p}$ curves appear more closely packed together. The $\tilde{c_p}$ values tend to vary more at lower velocities, but the maximum variation range of ± 0.012 is respected for velocities between 15 m/s and 20 m/s.

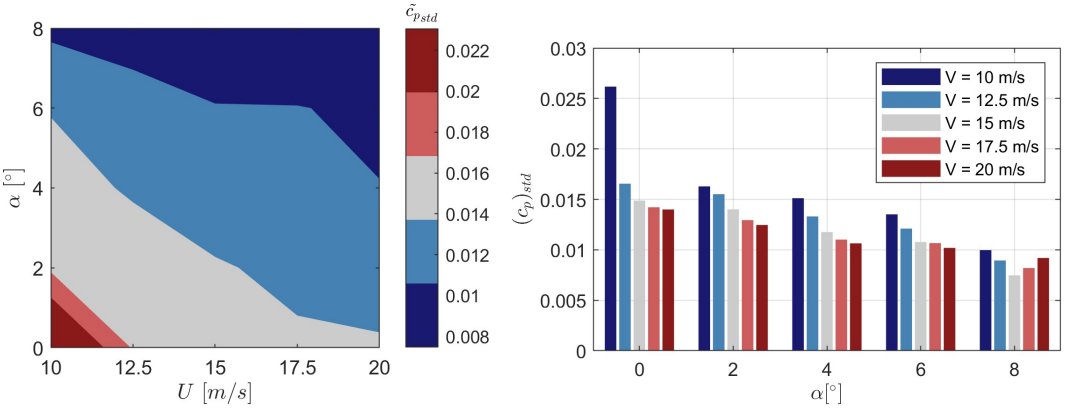

(a) (b)

Figure 3.6: Standard deviation of the non-dimensional pressure coefficient $\tilde{c}_{p_{std}}$ at different flow speeds and flap deflection angles in map representation (a) and bar chart representation (b)

With the goal of summarizing the effect of the flap deflection angle and of the flow velocity on the presence of pressure gradients along the flat plate, the standard deviation of the $\tilde{c_p}$ coefficient was employed. In figure 3.6 the standard deviation of the non-dimensional pressure coefficient for the tested velocities and flap deflection angles is shown in map form and in bar chart form. It can be observed that the $\tilde{c_p}$ always tends to experiment lower variations for higher flap deflection angles α and higher flow velocities.

3.3 Boundary layer behavior

To validate the new flat plate setup, an extensive investigation on the correct behavior of the zero pressure gradient turbulent boundary layer have been conducted. The boundary layer measurements presented in this section have been taken by the hot wire anemometry measurement system described in paragraph 2.2.2, using a sampling frequency of 50 kHz and a sampling time of 30 s. The experimental data of an hot wire measured boundary layer consists in a set of mean velocity and root mean square of the velocity fluctuations value, together with their relative wall normal measurement position y. To

obtain accurate values of the wall position is one of the main challenges of conducting hot wire measurements in turbulent boundary layers; at the same time, an accurate evaluation of the wall position is crucial to obtain reliable information from the study of the velocity profiles. For this reason, the experimental data has been subjected to post-processing through a MATLAB written optimization algorithm, in which a wall distance correction will be determined, together with the boundary layer's characteristic parameters. The used optimization algorithm is described in the appendix A.

3.3.1 Development of the boundary layer in the leading edge proximity

Numerous boundary layer acquisitions have been conducted close to the flat plate's leading edge ($x = 0.395\,m$) to examine both the natural boundary layer transition and the uniformity of the flow generated by the trip devices.

Boundary layer transition:

With no turbulence tripping structures installed, measurements at different flow velocities have been carried out to estimate the transitional Reynolds number of the experimental facility.

$U_\infty\,[m/s]$	8.3	11.9	16.3	20.9
Re_x	220000	315000	430000	550000
Re_θ	350	400	500	1100
$\delta\,[m]$	0.0043	0.0041	0.0035	0.0083
$\delta^*\,[m]$	0.0013	0.0011	0.0009	0.0011
$\theta\,[m]$	0.0006	0.0005	0.0005	0.0008
H	2.13	2.11	1.93	1.38
$\tau\,[Pa]$	0.04	0.08	0.12	0.45
c_f	0.0010	0.0009	0.0007	0.0017

Table 3.1: Boundary layer parameters for different velocities at $x = 0.395\ m$.

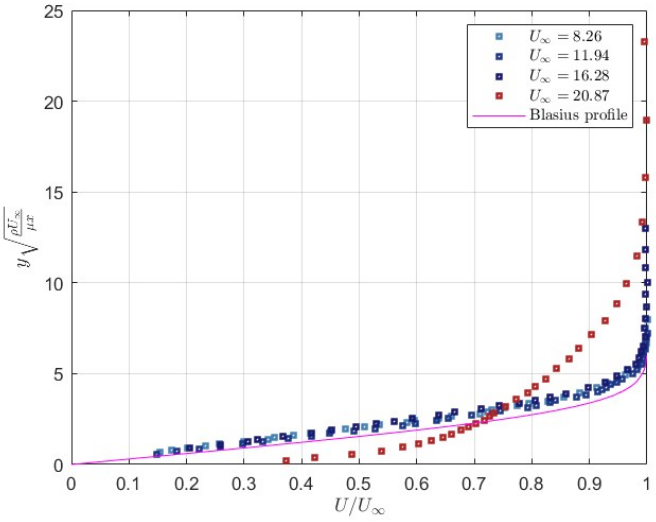

Figure 3.7: Boundary layer velocity profiles in the Blasius scaling at different velocities

In figure 3.7 the boundary layer profiles are compared in the Blasius scaling; it can be seen that the boundary layer profile at $U_\infty = 20.9\,m/s$ retains the turbulent characteristics. The same can be observed by comparing the values of the shape factor H, the skin friction coefficient c_f and the boundary layer thickness δ, in table 3.1. It can then be assumed that the transitional Reynolds number is between 430000, corresponding to $U_\infty = 16.3\,m/s$ and 550000, corresponding to $U_\infty = 20.9\,m/s$.

Near field development of the artificially generated turbulent boundary layers:

Following the work of Rodrìguez-Lòpez, Bruce and Buxton (2016) [7], boundary layer acquisitions have been conducted in the proximity of the trip devices to examine the near field development of the turbulent boundary layers generated by the two selected turbulence tripping structures. Two acquisitions, one behind an obstacle and one behind a gap, have been performed for both the trips at a free stream velocity of $10m/s$. The observations have been conducted at approximately 0.2 m from the trips, which, in turn, were placed at $x \simeq 0.2\ m$ from the flat plate's leading edge. The results are presented in non-dimensional form, as the vertical coordinate will be scaled with the trip's height ($\hat{y} = y/h$) and the velocities with the freestream speed ($\hat{u} = u/U_\infty$).

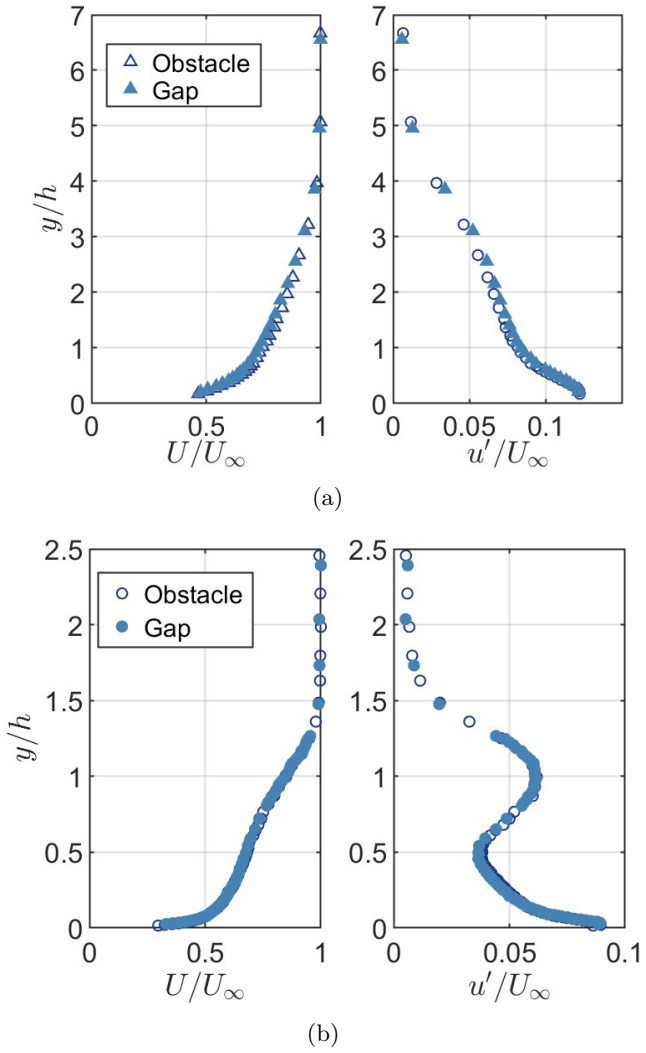

Figure 3.8: (a,c) mean $\hat{u}$ and (b,d) $\hat{u'}$ velocity profiles for (a,b) the "sawtooth" trip, (c,d) the "2row20" trip

Figure 3.20a shows that both the mean velocity and velocity fluctuations profiles of the turbulent boundary layer generated by the "sawtooth" type trip, which introduces smaller disturbance on the flow, appear to retain the canonical shape. The "2row20" type trip (figure 3.20a), on the other hand, generates thicker turbulent boundary layers whose structure is initially highly altered. This is due to the tripping structure's bigger dimensions and consequent bigger disturbance on the flow, which is strongly affected by the vortices shed by the trip's vertical cylinders on which the turbulence tripping mechanism is based. This is particularly clear when observing the velocity fluctuations profiles, which show a second peak of turbulence production at $y = h$ ($\hat{y} = 1$),

due to the shear layer introduced by the interaction between the trip induced shedding and the freestream [7].

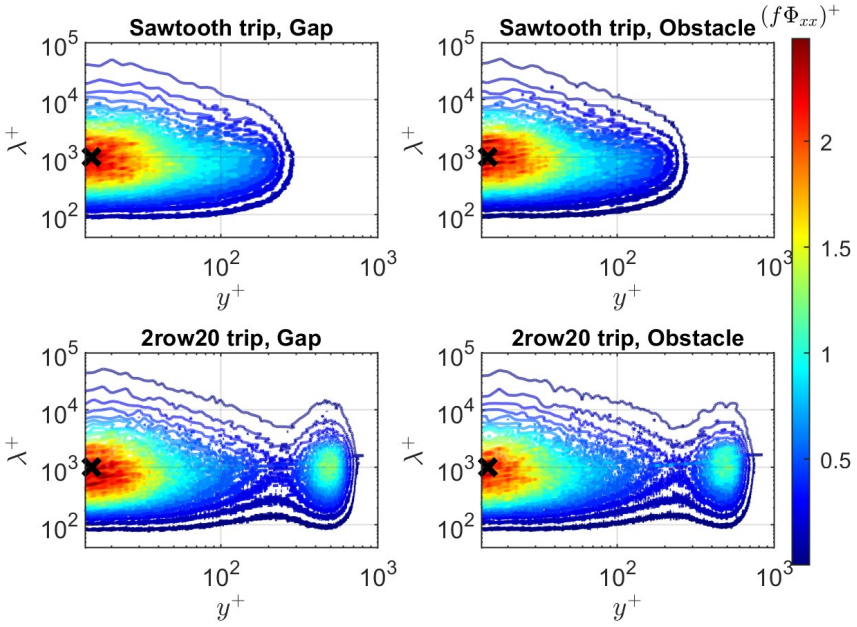

Figure 3.9: Contour plots of pre-multiplied spectra of the streamwise velocity, normalized in wall units ($f\Phi_{xx}/u_\tau^2$). The black crosses represent the expected location of the buffer layer ($y^+ = 15$, $\lambda^+ = 1000$)

The pre-multiplied spectra contours for the two tripping structures in the two positions are shown in figure 3.9. This visualizations show the distribution of the energy content across the frequency field. The pre-multiplied spectra is defined as $(f\Phi_{xx})$, where Φ_{xx} is the power spectral density of the velocity fluctuations, and is normalized by u_τ^2. The wavelength λ was evaluated by applying Taylor's hypothesis, that is converting the frequencies into wavelengths by calculating the space traveled by the signal at an advection velocity U_a, and using the local mean streamwise velocity as advection velocity:

$$\lambda(y^+) = U(y^+) \cdot T = \frac{U(y^+)}{f}$$

In the contour plots, the expected location of the peak of turbulent energy is highlighted. The peak should be located at $y^+ \approx 15$, corresponding to the buffer layer position, and the normalized wavelength should take the value of $\lambda^+ \approx 1000$ [25], which correspond to the canonical length of the low speed streaks [8]. The "sawtooth" trips perfectly reproduces the expected position of the peak, while the "2row20" trip's peak seem to be located at a slightly lower value of λ^+. It can be seen that the spectra of the "2row20" trips shows a

second peak at $y^+ \approx 500$. This is the peak related to the shear layer produced by the interaction between the the trip induced shedding and the freestream [7]. The resulting turbulent structures feature a slightly larger wavelength ($\lambda \approx 1100$) compared to that of the inner peak.

3.3.2 Boundary layer development along the flat plate

Boundary layer acquisitions have been made at two different upstream velocities ($U_{x=0.395\,m} \simeq 10\ m/s$, $U_{x=0.395\,m} \simeq 20\ m/s$) in 4 different positions along the flat plate axis ($x = 0.395\,m$, $x = 1.065\,m$, $x = 1.735\,m$, $x = 2.405\,m$) in the case of natural transition of the boundary layer and for both the tripping structure types. This study has allowed to observe the boundary layer natural development and to compare it's behavior with that of the turbulent boundary layers produced by the turbulence tripping with the two different devices.
In the figures that will be reported in this section, the marker's main color will represent the lower inlet velocity cases(blue) and the higher inlet velocity cases (red), while the shades of the main color will represent the locations along the flat plate (lighter shades for more upstream positions, darker shades for more downstream positions). Finally, the marker type will represent a different type of boundary layer development (squares for the natural development, triangles for the "sawtooth" trip, circles for the "2row20" trip.

Naturally developed boundary layer

The boundary layer acquisitions taken with no turbulence tripping structure installed allowed to highlight the discontinuity in the boundary layer thickness development which appears when the the flow transitions form laminar to turbulent. The boundary layers observed for 10 m/s inlet velocity showed laminar characteristics until $x = 1735\ mm$ and then became turbulent at $x = 2405\ mm$. This can be observed in figure 3.10a or by the change in the value of the H parameter presented in table 3.2, as well as by the shift in the value of the skin friction coefficient. The inner-scaled mean streamwise velocity profile and the velocity fluctuations variance for the higher velocity case are reported in figure 3.20. The theoretical laws of the viscous sublayer and logarithmic layer are reported for comparison. The generally accepted values of $k = 0.384$, $B = 4.17$ [16] have been used for the logarithmic law.

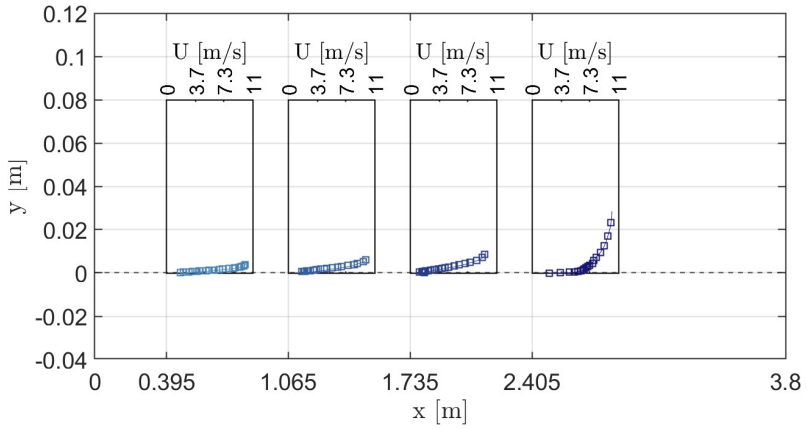

(a)

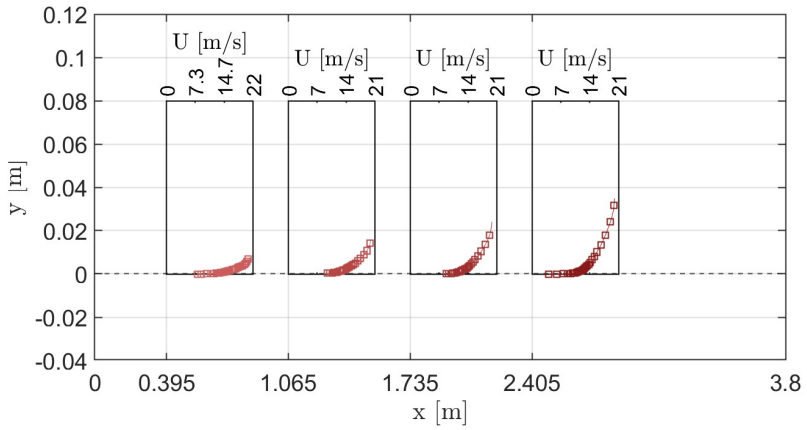

(b)

Figure 3.10: Evolution of the dimensional velocity profile of the boundary layer in the case of natural transition for (a) the lower tested velocity ($U_{x=0.395\,m} \simeq 10\ m/s$), (b) the higher tested velocity ($U_{x=0.395\,m} \simeq 20\ m/s$)

$U_{x=0.395\,m} = 10.2$ m/s				
	$x = 0.395$ m	$x = 1.065$ m	$x = 1.735$ m	$x = 2.405$ m
$U_\infty\,[m/s]$	10.2	10.1	9.6	10.2
Re_x	270000	700000	1100000	1600000
Re_θ	430	600	830	1920
$\delta\,[m]$	0.0043	0.0071	0.0100	0.0290
$\delta^*\,[m]$	0.0012	0.0018	0.0028	0.0038
$\theta\,[m]$	0.0006	0.0009	0.0013	0.0028
H	1.90	2.04	2.17	1.347
$\tau_w\,[Pa]$	0.07	0.04	0.03	0.24
c_f	0.0010	0.0006	0.0006	0.0038
Re_τ	–	–	–	850
Π	–	–	–	0.31
$u_\tau\,[m/s]$	–	–	–	0.44
$U_{x=0.395\,m} = 20.9$ m/s				
	$x = 0.395$ m	$x = 1.065$ m	$x = 1.735$ m	$x = 2405$ m
$U_\infty\,[m/s]$	20.9	20.0	19.8	20.0
Re_x	550000	1400000	2260000	3200000
Re_θ	1090	2530	3330	5270
$\delta\,[m]$	0.0075	0.0160	0.0243	0.0350
$\delta^*\,[m]$	0.0011	0.0024	0.0034	0.0054
$\theta\,[m]$	0.0008	0.0019	0.0026	0.0040
H	1.38	1.29	1.33	1.37
$\tau_w\,[Pa]$	1.07	0.81	0.76	0.68
c_f	0.0041	0.0034	0.0032	0.0028
Re_τ	470	880	1280	1760
Π	0.37	0.49	0.59	0.64
$u_\tau\,[m/s]$	0.94	0.82	0.79	0.75

Table 3.2: Boundary layer parameters for different positions along the flat plate at different velocities in the case of natural transition.

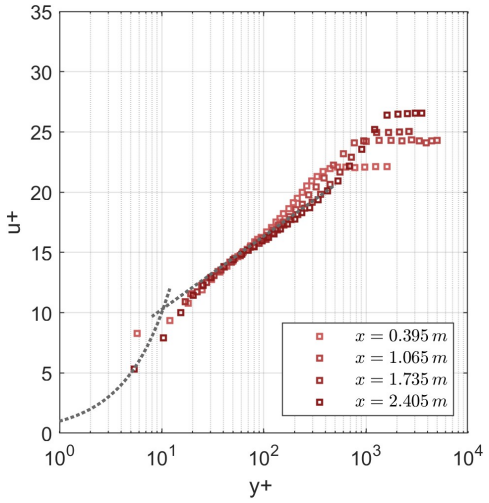

(a)

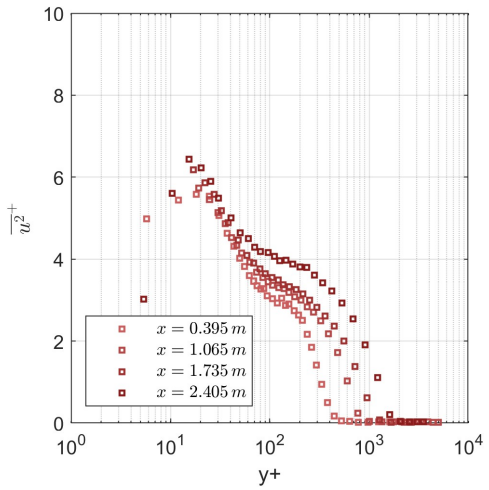

(b)

Figure 3.11: Evolution of inner scaled mean streamwise velocity (a), velocity variance (b) at $U_{x=0.395m} \simeq 20\,m/s$ in the case of natural transition

Sawtooth trip

The turbulent boundary layers obtained by installing the "sawtooth" trip show larger thickness compared with the ones obtained with the natural transition. This is more evident at the lower inlet velocity, as can be observed in figure 3.12a or by the data reported in table 3.3.

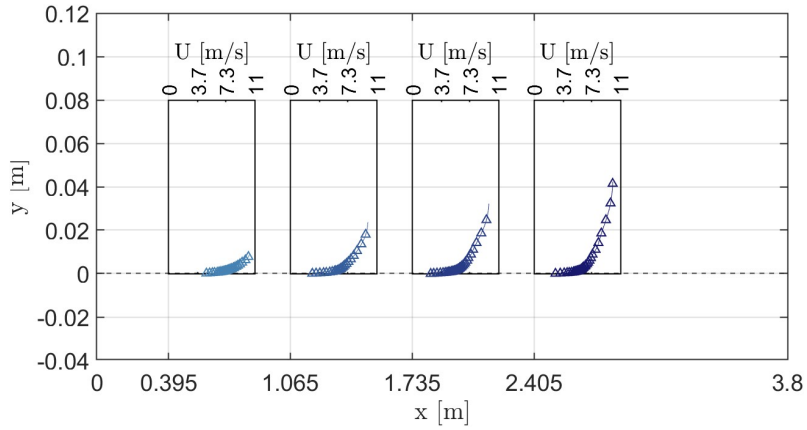

(a)

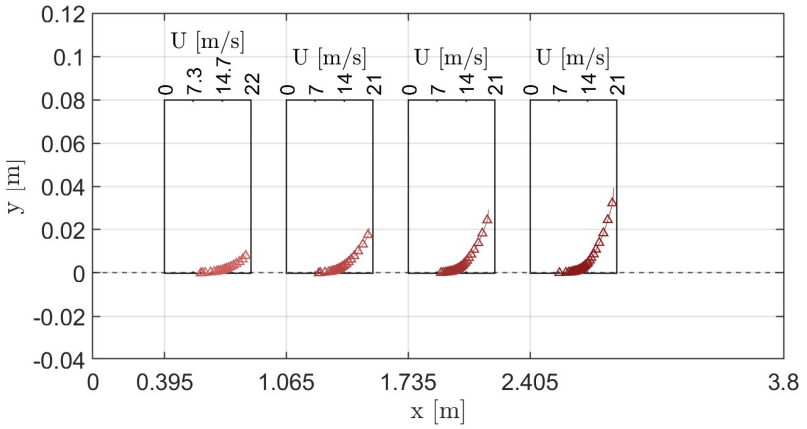

(b)

Figure 3.12: Evolution the dimensional velocity profile of the boundary layer using the "sawtooth" type trip for (a) the lower tested velocity ($U_{x=0.395m} \simeq 10\,m/s$), and (b) the higher tested velocity ($U_{x=0.395m} \simeq 20\,m/s$)

$U_{x=0.395\,m} = 10.3$ m/s				
	$x = 0.395$ m	$x = 1.065$ m	$x = 1.735$ m	$x = 2.405$ m
$U_\infty\,[m/s]$	10.3	9.9	9.8	10.0
Re_x	270000	700000	1100000	1600000
Re_θ	680	1780	2460	3170
$\delta\,[m]$	0.0091	0.0239	0.0324	0.0425
$\delta^*\,[m]$	0.0013	0.0037	0.0054	0.0064
$\theta\,[m]$	0.0010	0.0027	0.0038	0.0048
H	1.32	1.38	1.41	1.36
$\tau_w\,[Pa]$	0.16	0.21	0.19	0.20
c_f	0.0025	0.0037	0.0032	0.0032
Re_τ	300	680	850	1140
Π	0.34	0.62	0.70	0.52
$u_\tau\,[m/s]$	0.50	0.42	0.39	0.40
$U_{x=0.395\,m} = 21$ m/s				
	$x = 0.395$ m	$x = 1.065$ m	$x = 1.735$ m	$x = 2.405$ m
$U_\infty\,[m/s]$	21.0	20.2	19.5	20.4
Re_x	550000	1400000	2250000	3300000
Re_θ	1500	3540	4330	5910
$\delta\,[m]$	0.0097	0.0211	0.0294	0.0394
$\delta^*\,[m]$	0.0015	0.0036	0.0046	0.0058
$\theta\,[m]$	0.0011	0.0026	0.0034	0.0044
H	1.37	1.36	1.35	1.34
$\tau_w\,[Pa]$	0.97	0.72	0.66	0.70
c_f	0.0037	0.0029	0.0029	0.0028
Re_τ	580	1090	1460	2000
Π	0.52	0.72	0.68	0.63
$u_\tau\,[m/s]$	0.90	0.77	0.74	0.76

Table 3.3: Boundary layer parameters for different positions along the flat plate at different velocities in the case of the "sawtooth" trip use

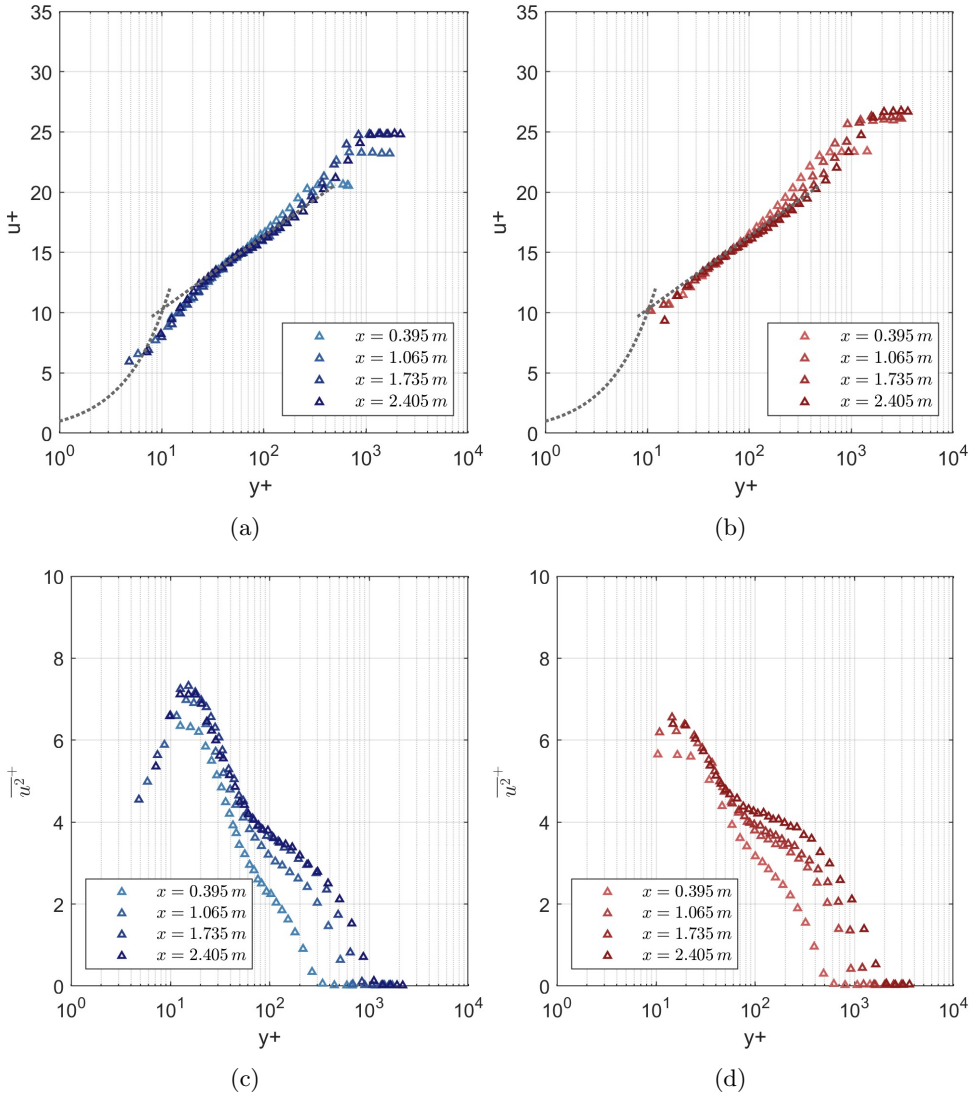

Figure 3.13: Evolution of inner scaled mean streamwise velocity (a,b), and velocity variance (c,d) at $U_{x=0.395m} \simeq 10\,m/s$ (a,c) and $U_{x=0.395m} \simeq 20\,m/s$ (b,d), in the case of the "saw-tooth" trip use

2row20 trip

The "2row20" trip produces much thicker turbulent boundary layers when compared to the "sawtooth" trip. However, the turbulent boundary layer characteristic parameters, especially the form factor H and the wake parameter Π, reported in table 3.4 present non-canonical values. The variance of the velocity fluctuations also does not present the typical shape in the first x measurement positions, as shown in figure 3.15

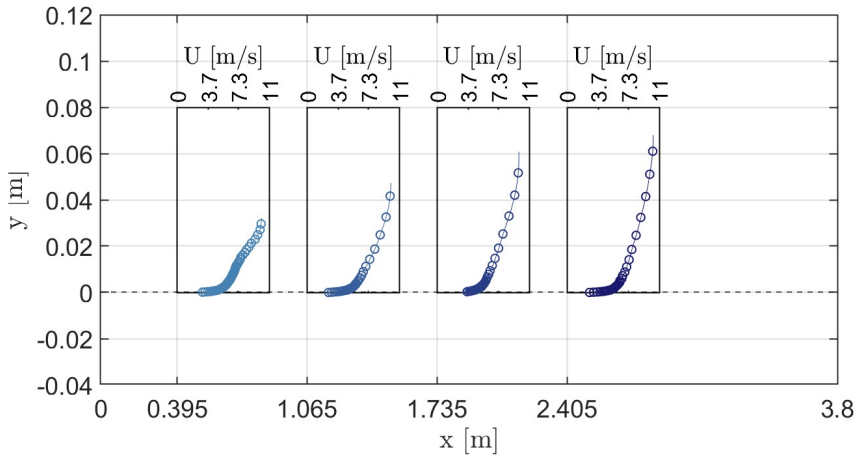

(a)

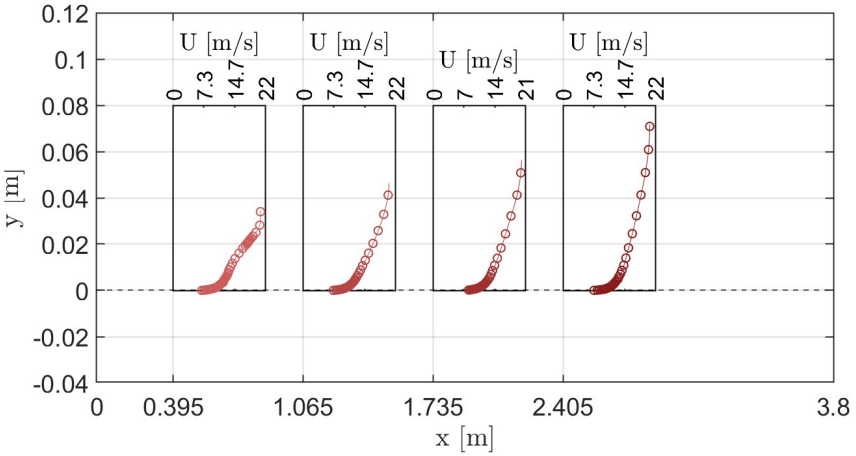

(b)

Figure 3.14: Evolution of the dimensional velocity profile of the boundary layer using the "2row20" type trip for (a) the lower tested velocity ($U_{x=0.395\,m} \simeq 10\ m/s$), (b) the higher tested velocity ($U_{x=0.395\,m} \simeq 20\ m/s$)

$U_{x=0.395\,m} = 10.1$ m/s				
	$x = 0.395$ m	$x = 1.065$ m	$x = 1.735$ m	$x = 2.405$ m
$U_\infty\,[m/s]$	10.1	10.0	9.7	10.3
Re_x	270000	710000	1100000	1600000
Re_θ	3270	3910	4650	5630
$\delta\,[m]$	0.0324	0.0474	0.0608	0.0680
$\delta^*\,[m]$	0.0072	0.0085	0.0105	0.0114
$\theta\,[m]$	0.0048	0.0059	0.0073	0.0082
H	1.49	1.45	1.44	1.39
$\tau_w\,[Pa]$	0.16	0.16	0.15	0.17
c_f	0.0026	0.0026	0.0026	0.0027
Re_τ	800	1150	1420	1730
Π	1.15	1.00	1.05	0.74
$u_\tau\,[m/s]$	0.37	0.37	0.35	0.38
$U_{x=0.395\,m} = 20.8$ m/s				
	$x = 0.395$ m	$x = 1.065$ m	$x = 1.735$ m	$x = 2.405$ m
$U_\infty\,[m/s]$	20.8	20.5	20.1	20.7
Re_x	550000	1500000	2300000	3300000
Re_θ	7030	8400	9300	11600
$\delta\,[m]$	0.0348	0.0465	0.0565	0.0718
$\delta^*\,[m]$	0.0078	0.0087	0.0097	0.0115
$\theta\,[m]$	0.0051	0.0061	0.0070	0.0084
H	1.53	1.43	1.39	1.36
$\tau_w\,[Pa]$	0.54	0.55	0.57	0.61
c_f	0.0021	0.0022	0.0023	0.0024
Re_τ	1540	2110	2600	3400
Π	1.54	1.19	0.96	0.79
$u_\tau\,[m/s]$	0.67	0.68	0.69	0.71

Table 3.4: Boundary layer parameters for different positions along the flat plate at different velocities, in the case of the "2row20" trip use

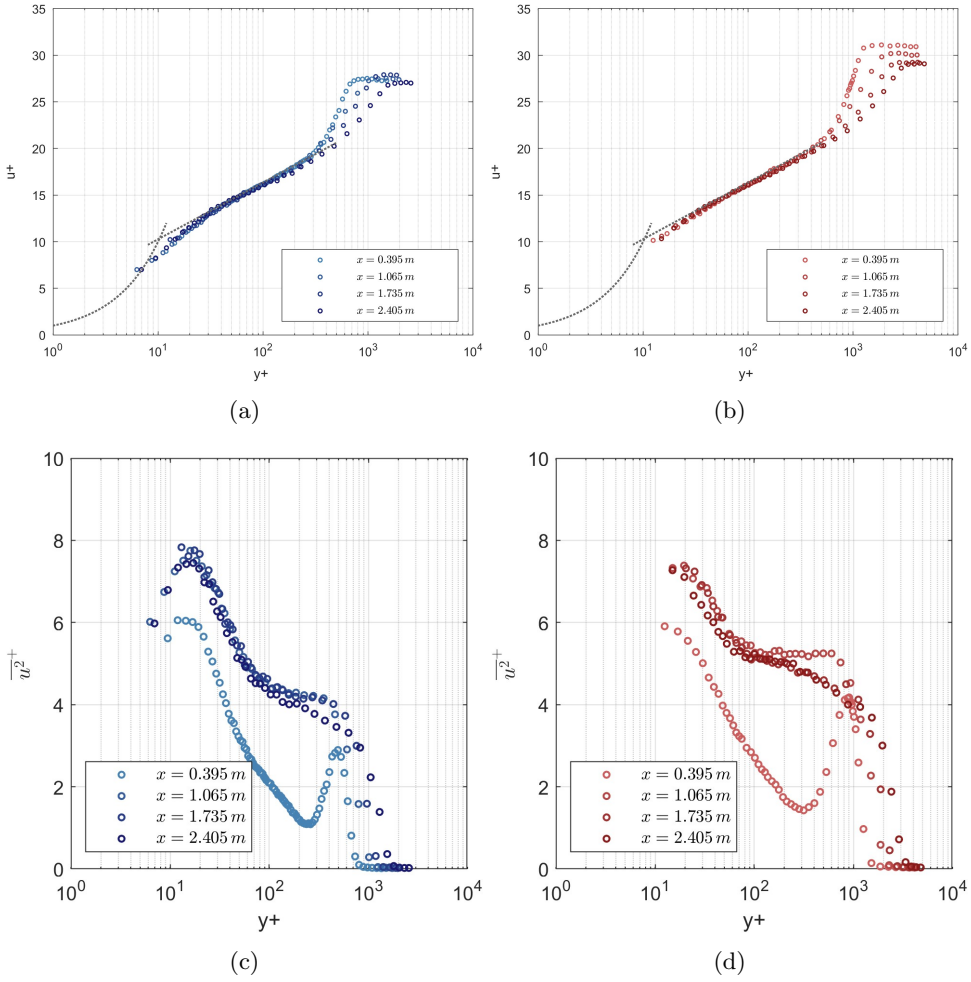

Figure 3.15: Evolution of inner scaled mean streamwise velocity (a,b), and velocity variance (c,d) at $U_{x=0.395m} \simeq 10\,m/s$ (a,c) and $U_{x=0.395m} \simeq 20\,m/s$ (b,d), in the case of the "2row20" trip use

3.3.3 Analysis of the observations with diagnostic plot approach

The results given by the boundary layer acquisitions for both the natural transition and the artificial transition cases have then been validated through the diagnostic plot approach. This diagnostic criterion has been introduced by Alfredsson, Segalini and Orlu [26] and has the great advantage of being independent from the accuracy of the determination of the absolute wall position y or of the friction velocity u_τ. In the diagnostic plot method, the only needed experimental quantities are U, the mean streamwise velocity, and u', the velocity fluctuations. The root mean square of the velocity fluctuations u' get scaled by the corresponding values of U and are plotted against the mean streamwise velocity U normalized by the freestream velocity U_∞. In this scaling, the data

for canonical zero pressure gradient boundary layers should collapse in the outer region, especially for $0.7 < U/U_\infty < 0.9$, following the linear relation:

$$\frac{u}{U_\infty} = \alpha - \beta \frac{U}{U_\infty} \tag{3.1}$$

Where the coefficients α and β assume the empirical values of $\alpha = 0.280$ and $\beta = 0.245$ for $Re_\theta > 2000$.
The evolution of the skin friction coefficient c_f with Re_θ has also been reported, to relate the respect of the diagnostic plot scaling to the agreement of the skin friction values with the Coles–Fernholz relation [12]:

$$2 \cdot \left[\frac{1}{k} ln(Re_\theta) + C) \right]^{-2} \tag{3.2}$$

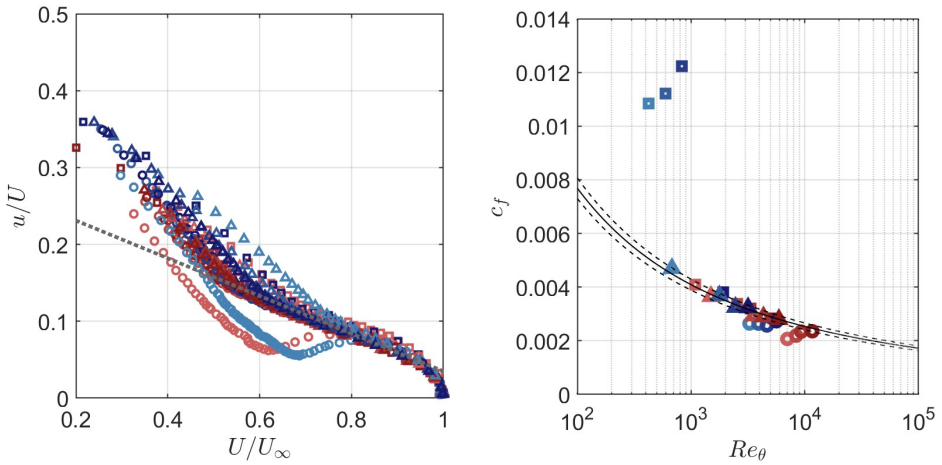

(a) (b)

Figure 3.16: (a) Diagnostic plot and (b) skin friction c_f evolution with Re_θ for all the tested cases. Squares represent the naturally developed boundary layers, triangles represent the "sawtooth" trip results and circles the "2row20" results. Shades of blue represent the lower velocity cases and shades of red the high velocity cases. In (a), the dashed line represents the linear relation 3.1, which applies to the $0.7 < U/U_\infty < 0.9$ range. In (b), the solid line represents the 3.2 relation and the dashed line represent a ±5% deviation. The c_f data from the laminar boundary layers in the case of natural transition at the lower tested velocity is added in (b).

The linear fitting of the experimental data provided the values of α and β. The coefficients obtained have then been compared with the $\alpha = 0.280$ and $\beta = 0.245$ empirical values and the turbulent boundary layers acquisitions whose coefficients didn't fall in the canonical values with a ±5% tolerance have been excluded.

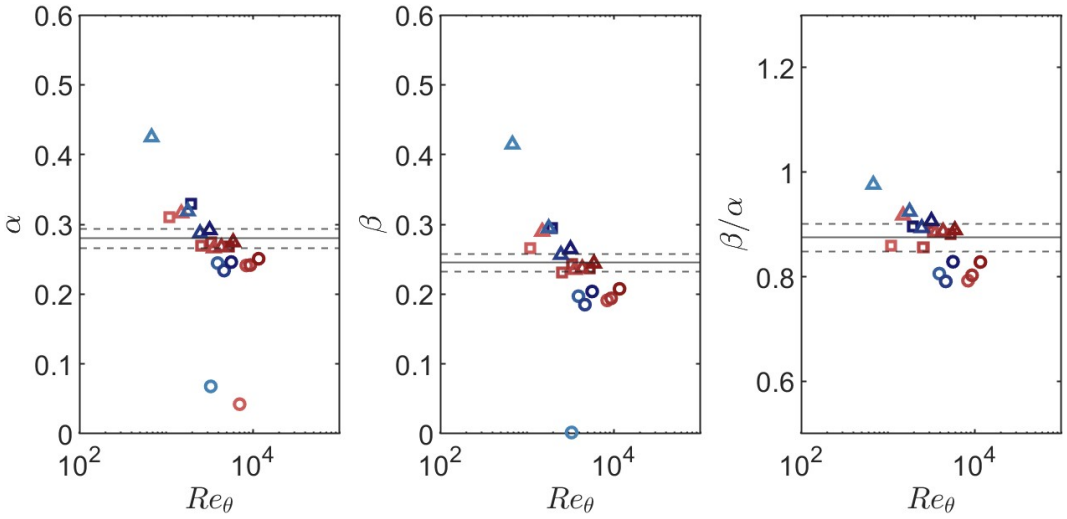

Figure 3.17: α and β coefficients of the interpolating first order polynomial of the experimental data at the various Re_θ values of the corresponding boundary layers

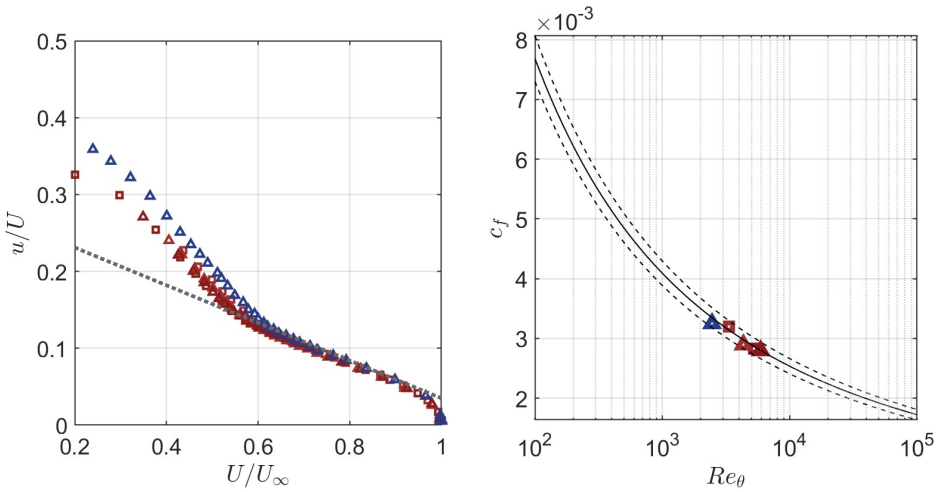

(a) (b)

Figure 3.18: (a) Diagnostic plot and (b) skin friction c_f evolution with Re_θ for the tested cases which respected the diagnostic plot scaling

In figure 3.18 the boundary layer measurements which follow the diagnostic plot scaling are shown. It can be observed that the skin friction coefficient obtained with the post processing algorithm from the velocity profiles falls into the $\pm 5\%$ deviation around the values predicted by the Coles–Fernholz relation. It should be noted that the measurements that respected the diagnostic plot scaling correspond to x measurements positions farther from the leading edge and that none of the high Reynolds number turbulent boundary layers generated by the "2row20" trip respected the diagnostic plot scaling, though seeming to recover the well-behaved characteristics at increasing distances form the turbulence tripping device.

3.3.4 Boundary layer behavior on the riblet test station

As explained in paragraph 2.4, the use of floating test plates, which is necessary to carry out force measurements through displacement measurements by LVDT sensors, introduces some issues that could affect the boundary layer structure. The gap between the flat plate and the smaller tile where the measurements will be conducted could, in fact, be a source of air leakage, while the misalignment of the testing plate with the surrounding flat plate could introduce surface discontinuities and thus have an impact on the flow's spanwise uniformity.
Even though the force measurement floating system was not employed in this work, the functioning of the plate alignment and sealing systems described in paragraph 2.4.1 have been tested by recreating a 3 mm gap, compatible with the floating system operating conditions.
Boundary layer acquisitions for the three different turbulence tripping structures have been conducted at the three positions showed in figure 3.19 to reveal the effect of the gap. "A" corresponds to 46 mm upstream the gap, "B" to 34 mm downstream the gap, while "C" is in the center of the testing plate. The measurements were conducted at 15 m/s flow external speed.

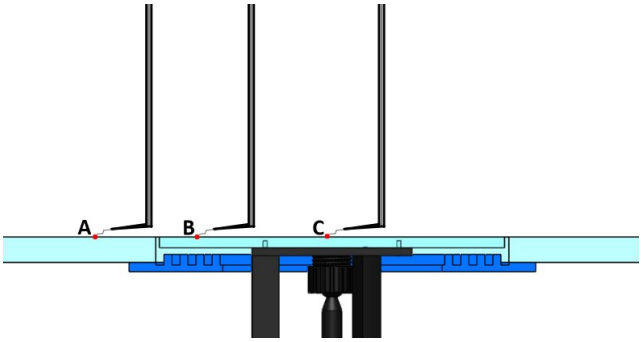

Figure 3.19: Measuring positions across the interface between the flat plate and the testing plate

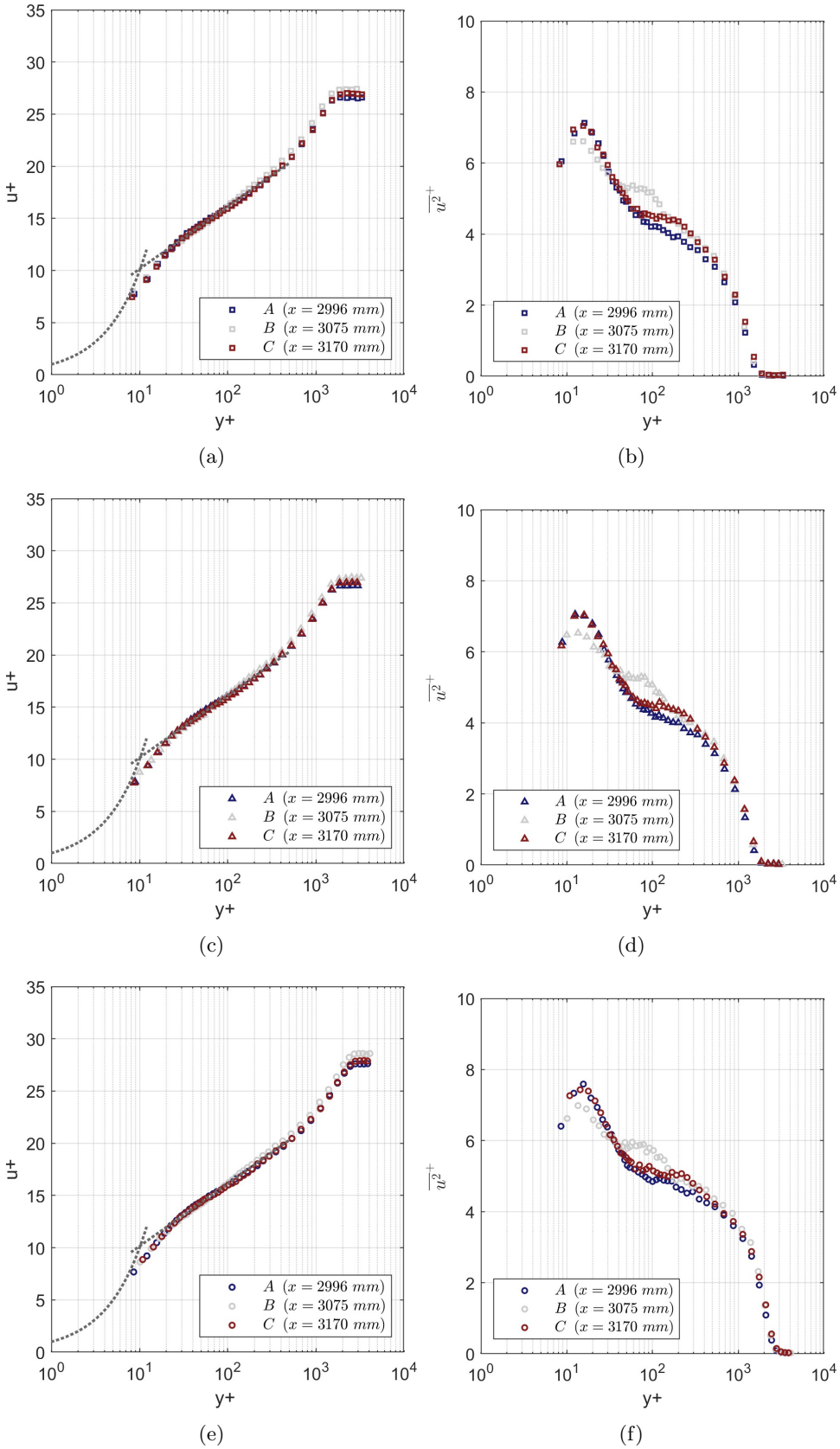

Figure 3.20: Evolution of inner scaled mean streamwise velocity profiles (a,c,e) and velocity variance (b,d,f), for (a,b) the case of natural transition (c,d) the "sawtooth" trip, (e,f) the "2row20" trip

In all the tested cases a slight modification of the boundary layer structure has been observed in the measuring position immediately after the 3 mm gap ($x = 3075\ mm$). The most evident feature of the altered boundary layer is the presence of a bump in the velocity fluctuations variance profiles, located around $40 < y^+ < 150$, corresponding to the logarithmic layer existence region. A lower value of the peak velocity fluctuations variance is also observed. The post-processing optimization algorithm for the determination of the boundary layer parameters has also provided a lower value of the intercept of the logarithmic layer's expression, B, suggesting that the boundary layer's velocity profile has been in some way slightly shifted down in the near proximity of the gap. These effects have been attributed to some residual flow leakage through the gap, which introduces similar features to those of suctioned boundary layers.
The turbulent boundary layer regains its canonical characteristics at the plate's center ($x = 3170\ mm$): the peak of the velocity fluctuations variance shares its value with that measured upstream the gap, the k and B constants of the logarithmic region's expression regains the canonical values of $k = 0.384$ and $B = 4.17$ and the velocity fluctuations bump observed immediately downstream the gap disappears. The only notable difference with respect to the boundary layer upstream the gap appears to be a slight deviation of the velocity fluctuations variance profiles at $y^+ > 100$. As reported in figure 3.21, all the measured boundary layers, including those immediately downstream the gap, appear to adhere to the diagnostic plot scaling.

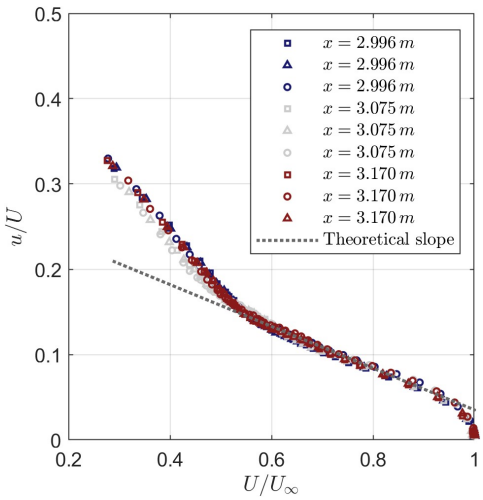

Figure 3.21: Diagnostic plot for all the boundary layer measurements across the gap. The different colors represent the different positions A,B and C. The marker type indicates the applied turbulence tripping.

Chapter 4

Results: boundary layer observations on riblets

In this chapter, the observations of the riblet manipulated turbulent boundary layers will be presented. This study has involved only the use of hot wire anemometry measurements; therefore, the drag reduction will be evaluated only locally and through the analysis of the mean streamwise velocity profiles. Furthermore, the topology of the turbulent structures cannot be resolved; hence, the study will focus on the effect of riblets on the mean streamwise velocity profiles and on the analysis of the distribution of the turbulent energy across the length scales. The observations have been made on the conventional longitudinal riblets and on the smaller amplitude sinusoidal riblets used in [8, 9]. The longitudinal riblets will be called "Rlong" and the sinusoidal riblets "Rs1" for brevity. Both the riblet configurations feature parabolic shaped groves with $s = 300\ \mu m$ spacing and $h = 210\ \mu m$ crest height. The geometric parameters of the two observed tested plates are reported in table 4.1

	Rlong	*Rs1*
$s\,[mm]$	0.30	0.30
$h\,[mm]$	0.21	0.21
h/s	0.7	0.7
$a\ [mm]$	0	0.15
$\lambda_{rib}\ [mm]$	∞	19.2
N_λ	0	13

Table 4.1: Geometric data for the two tested riblet configurations

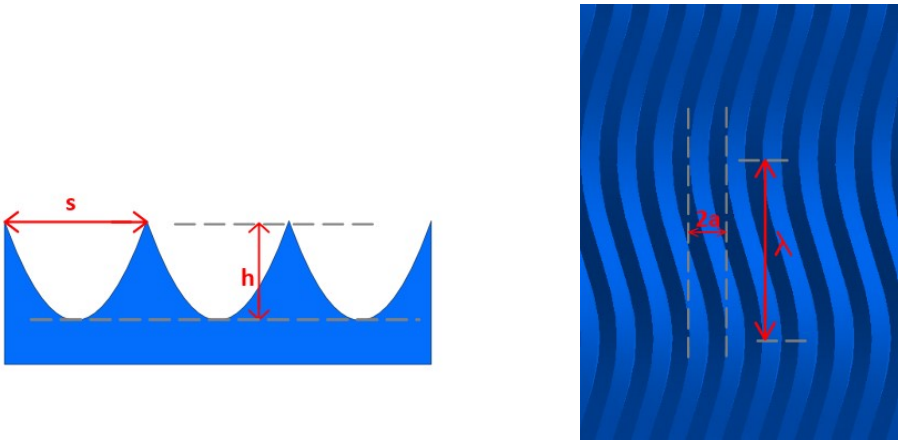

(a) (b)

Figure 4.1: Schematic representation of the geometry of the tested riblet configurations. Both the "Rlong" type riblets and the "Rs1" type riblets share the same parabolic shape of the grooves.

4.1 Drag reduction curve and flow field analysis

Boundary layer acquisitions on the two different tested plates have been performed at different flow velocity to investigate the drag reduction variation with the flow regime. The two riblet equipped testing tiles have been alternatively placed in the experimental setup and the flow velocity was set at three different values for the "Rlong" riblets and five different values for the "Rs1" riblets. This is equivalent to varying the riblet spacing in wall units s^+, as the viscous length scale, which normalizes the riblet spacing, varies with the flow's Reynolds number. Acquisitions on the smooth plate at the same flow velocities have been conducted to evaluate the drag reduction. The s^+ values have been calculated by using the viscous length scale obtained in the smooth plate case. The same post processing algorithm used for the previously presented acquisitions has been applied to the experimental data to obtain the boundary layer parameters for the smooth plate cases, while a modified algorithm was used for the riblet manipulated cases. In the modified algorithm, the k and Π constants, which should not be varied by the wall manipulation [10], have been kept fixed at the values obtained for the smooth plate. Conversely, the optimizer was given the freedom to generate optimized solutions in which the logarithmic region of the mean velocity profile is shifted away or towards the wall.
The results obtained from the experimental data analysis are reported in table 4.2 for the smooth plate case, in table 4.3 for the "Rlong" riblets and in table 4.4 for the "Rs1" riblets.

$U_\infty\,[m/s]$	$u_\tau\,[m/s]$	$l_\tau[\mu m]$	Re_θ	Re_τ	H
10.8	0.42	36	4340	1640	1.36
13.6	0.51	29.6	5410	1690	1.37
18.5	0.67	22.5	7350	2310	1.36
20.7	0.73	20.7	8150	2420	1.36
21.9	0.78	19.4	9320	3000	1.34

Table 4.2: Boundary layer parameters for the smooth plate case

$U_\infty\,[m/s]$	$u_\tau\,[m/s]$	$l_\tau[\mu m]$	Re_θ	Re_τ	H
10.9	0.42	36	4330	1720	1.36
13.6	0.48	31.5	5140	1800	1.35
18.5	0.65	23.2	7360	2370	1.37

Table 4.3: Boundary layer parameters for the "Rlong" riblets

$U_\infty\,[m/s]$	$u_\tau\,[m/s]$	$l_\tau[\mu m]$	Re_θ	Re_τ	H
10.8	0.41	36.8	4040	1640	1.36
13.60	0.49	30.8	4940	1770	1.35
18.5	0.64	23.6	6990	2320	1.37
20.7	0.72	21	8100	2610	1.34
21.9	0.78	19.4	8390	3000	1.34

Table 4.4: Boundary layer parameters for the "Rs1" riblets

The wall shear stress was calculated from the u_τ resulting from the optimization process described in appendix A. The results have been compared in terms of skin friction coefficient, thus normalizing the wall shear stress with $1/2\rho U^2$.

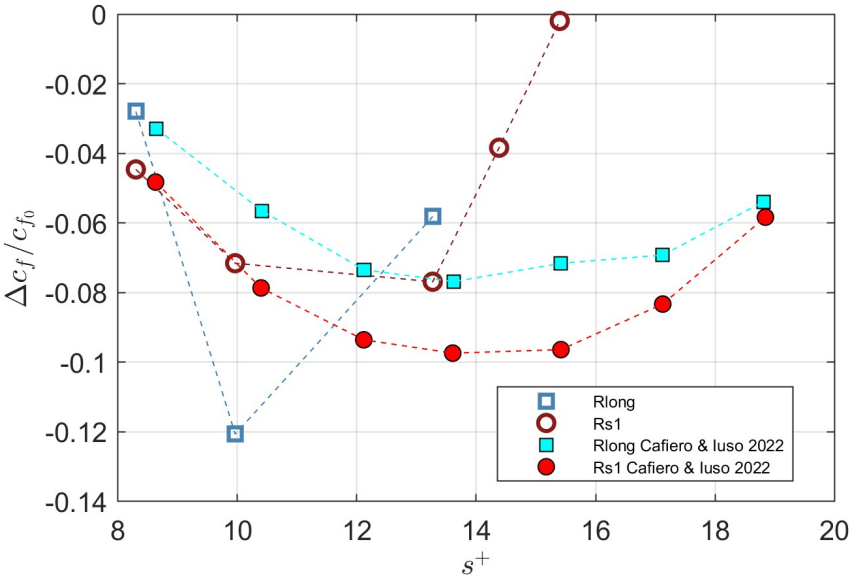

Figure 4.2: Skin friction coefficient relative variation $\Delta c_f/c_{f_0}$ with respect to the skin friction coefficient of the smooth plate at the same flow regime. The results obtained in [8] have been added for comparison. Note that the results reported in that article were obtained by load cells measurements, therefore the results have to be considered as "integrated" on the whole testing plate

In figure 4.2 the obtained drag reduction curve is reported. The results obtained by Cafiero and Iuso in [8] are added for comparison, although it should be kept in mind that the results reported in the article were obtained from load cell measurements and reported in terms of $\Delta c_D/c_{d0}$, thus representing "integral" force measurements on the entire testing plate. It can be seen that for low s^+ values the results obtained from the analysis of the velocity profiles agree well with those produced by load cell measurements, especially for the "Rs1" riblets. The value of drag reduction produced by the "Rlong" riblets at $s^+ \approx 10$ has been considered to be affected by issues in the post-processing of the data, since it falls outside of the well-established canonical range of values. The drag reduction at the optimal s^+ are slightly lower than the reference values in both cases, although the position of the maximum of drag reduction is confirmed. The additional observations on the "Rs1" riblets show a significant decrease of the drag reduction, which could be attributed to post-processing issues but also to the "local" nature of the measurements.
The non-dimensional mean streamwise profiles and the non-dimensional vari-

ance of the velocity fluctuations are reported, for $s^+ \approx 8.3$ and $s^+ \approx 13.3 \approx s^+_{opt}$, in figure 4.3

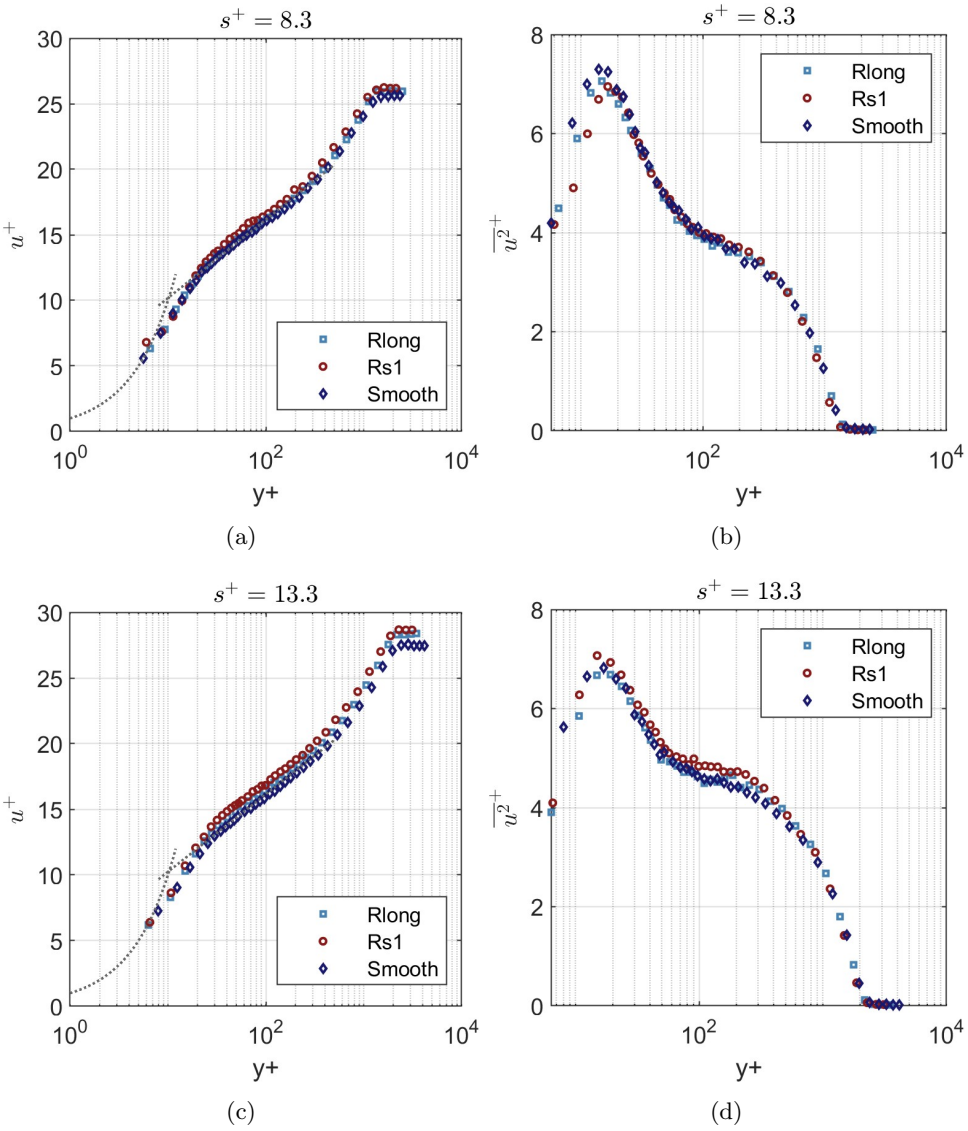

Figure 4.3: Non dimensional mean streamwise velocity profiles (a,c) and non dimensional variance of the velocity fluctuations (b,d) for $s^+ \approx 8.3$ (a,b) and $s^+ \approx 13.3 \approx s^+_{opt}$ (c,d)

The upward shift of the mean velocity profile is evident at $s^+ \approx 13.3 \approx s^+_{opt}$ for both the different riblets configurations. At $s^+ \approx 8.3$, which corresponds to a lower drag reduction, the upward shift is still present, but not as noticeable as in the maximum drag reduction case. Thus, it is clear that the drag reduction is related to how much the velocity profile is shifted away from the wall. As for the velocity variance, on the other hand, the effect of riblets does not ap-

pear to be noticeable; The dimensional velocity fluctuations are lower than in the smooth plate case, but the lower value of the friction velocity makes the normalized velocity variance overlap with the smooth plate results.

The velocity profile upward shift was expressed in terms of variation of the logarithmic layer's intercept B by Garcìa-Mayoral and Jimenéz in [10]:

$$\Delta c_f / c_{f_0} = \frac{\Delta B}{(2c_{f_0})^{-1/2} + (2k)^{-1}} \tag{4.1}$$

The obtained velocity profiles have been therefore compared to the logarithmic curves defined with the updated values of B.

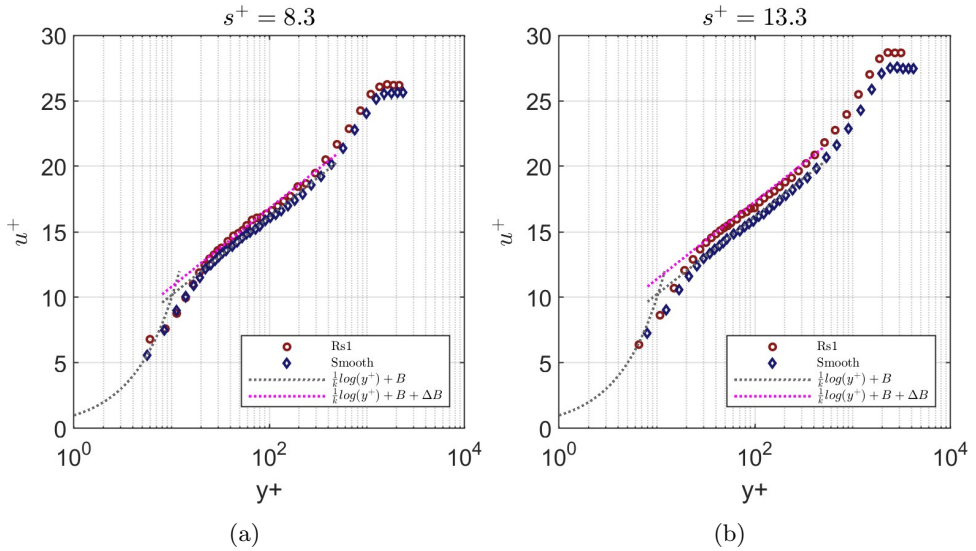

(a) (b)

Figure 4.4: Comparison of the experimental data obtained from the measurements on the "Rs1" riblets at $s^+ \approx 8.3$ (a) and $s^+ \approx 13.3$ (b) with the logarithmic law defined by the intercepts predicted by eq. 4.1

In figure 4.4 it can be observed that the obtained experimental results agree well with the logarithmic region's law defined by the intercept predicted by equation 4.1.

4.2 Velocity spectra analysis

To further understand the effect of riblets on the organization of the turbulent energy, the pre-multiplied spectra of the velocity fluctuations were computed. In line with [8], the pre-multiplied spectra has been calculated as $k_x \Phi_{xx}$, where k_x is the longitudinal wavenumber, that is $k_x = 2\pi/\lambda$. The wavelengths of the velocity fluctuations were, again, derived from the frequencies by applying the

Taylor's hypothesis and using the local mean streamwise velocity as advection velocity. The pre-multiplied power spectral density was then normalized with the square of the friction velocity.

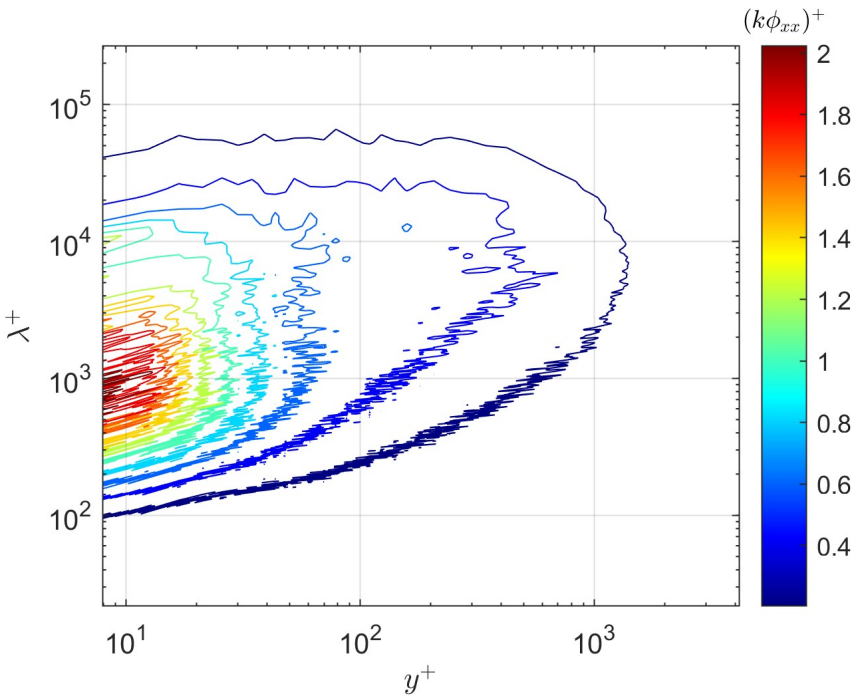

Figure 4.5: Contour of the inner scaled pre-multiplied spectra of the velocity fluctuations $k_x\Phi_{xx}/u_\tau^2$ measured on the smooth plate at the flow regime corresponding to the riblets maximum drag reduction

The pre-multiplied velocity spectra for the smooth plate case is reported in figure 4.5. The peak of turbulence production can be recognized at $y^+ \approx 15$, corresponding to the buffer layer location, and is characterized by wavelengths with values around $\lambda^+ = 1000$, which is the typical length of the near wall low speed streaks [8].
To highlight the reorganization of the turbulent energy, the results for the two riblet types have been represented as difference with respect to the smooth plate case:

$$\Delta(k_x\Phi_{xx})^+ = (k_x\Phi_{xx})^+ - (k_x\Phi_{xx})^+_{smooth}$$

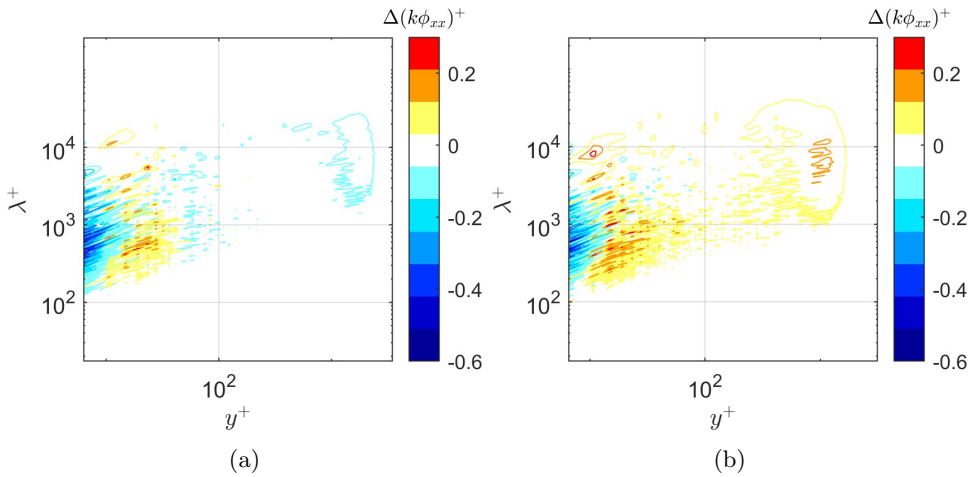

Figure 4.6: Contours of the difference, with respect to the smooth plate, of the pre-multiplied spectra of the velocity fluctuations $\Delta(k_x\Phi_{xx})^+$ of the riblet manipulated cases. (a) results for the "Rlong" riblets, (b) results for the "Rs1" riblets

Figure 4.6 shows the pre-multiplied spectra differences between the riblet cases and the smooth plate. Both the riblet measurements display a maximum of energy reduction in correspondence of the buffer layer location, where the energy peak was located in the smooth plate case. The new energy maximum resides at higher y^+, confirming the higher location of the region of maximum turbulent activity. The smaller wavelength values associated to the new maxima could also be attributed to the weakening of the turbulent structures by effect of the riblets [8, 9].

Chapter 5

Conclusions

The activities covered in this work have enabled the setup of an experimental facility that will support successful turbulence manipulation studies on riblets or other flow control techniques.
The design and assembly phases of the elements that completed the setup have been described. Then, the results of the preliminary characterization, with a focus on the requirements for the riblets studies in zero pressure gradient conditions, were reported. Finally, some observations of riblet manipulated turbulent boundary layers were discussed.

The first phase has included the assembly of the new flat plate, the design of a flap for the realization of the zero pressure gradient conditions, and the preparation of an adequate bi-directional probe positioning system. Two types of turbulence tripping structures have been selected and an alignment system was designed for the riblet testing plates.

The characterization of the wind tunnel revealed a slight asymmetry in the free stream flow, with a $\pm 0.4\%$ variation of the velocity on the tested section at 12 m/s mean velocity. A mean turbulence intensity level of $I = 0.7\%$ was found over the riblets testing station.

The pressure field observations revealed a good efficiency of the designed flap in reducing the local pressure gradients and in bringing to zero the non-dimensional pressure coefficient $\tilde{c_p}$ distribution. A map of the realizable operating conditions at various U_∞ and flap deflection angle α values was reported.

The study of the boundary layer through hot wire observations have provided indications on the development of the boundary layer in the leading edge proximity, where the critical Reynolds number for the boundary layer transition was estimated and the flow topology generated by the two different turbu-

lence tripping devices have been studied. The development of the boundary layer on the flat plate segment preceding the testing station was then studied by analyzing the inner scaled velocity profiles, the boundary layer parameters values and by using the recently proposed diagnostic plot approach. The more conventional "sawtooth" trip, characterized by a lower influence on the flow, provided satisfactory results, while the "2row20" trip provided artificial high Reynolds number turbulent boundary layers which did not prove to be "well behaved" in the most upstream measuring positions. The effect of the gap existing between the flat plate and the testing plate was then studied and the boundary layer flow was validated in the testing station.

The study of the riblet manipulated turbulent boundary layer has included the analysis of the mean streamwise velocity profiles and of the velocity fluctuations variance. The riblets drag reduction was evaluated by deriving the wall shear stress τ_w from the velocity profiles obtained in the post-processing of the hot wire data with the optimization algorithm described in appendix A. Some measurements did not yield the results obtained by load cell force measurements in previous studies. The vertical shift of the velocity profiles in the drag reducing cases was highlighted and the pre-multiplied spectra of the velocity fluctuations was then analyzed.

5.1 Future developments

The results obtained in this work provide an encouraging starting point for further developments of the experimental setup and for future turbulence manipulation studies.
One important upgrade of the experimental facility will be the addition of a force measurement system based on LVDT displacement sensors. This will enable to obtain reliable drag reduction measurements, which could also support the improvement of the optimization algorithm used. For this reason, the new components of the experimental setup described in this work were designed to be compatible with the LVDT force measurement system.
The experimental setup will also be upgraded with the addition of a pressure body to enable studies on riblet manipulated turbulent boundary layers in adverse pressure gradient conditions.
In conclusion, the experimental setup was designed to support particle image velocimetry (PIV) observations, therefore it would be interesting to support the local hot wire anemometry measurements with high spatial resolution flow field visualizations obtained by PIV techniques.

Appendix A

Post-processing of the experimental data of the boundary layer acquisitions

One of the main challenges when conducting boundary layer observations by hot wire anemometry measurements is to elaborate the experimental data for obtaining the main characteristic quantities of the flow. This include the boundary layer thickness δ, the momentum thickness θ and the displacement thickness δ^* and consequently the form factor $H = \delta^*/\theta$, the wall shear stress τ_w and others. In addition to that, with the exception of the integral quantities, the calculation of all of this parameters require an accurate determination of the wall position. The characteristic lengths involved in the near wall evolution of the mean velocity profiles are in fact significantly small, especially for turbulent boundary layers, making it really challenging to get the position of the first hot wire measurement point with respect to the wall. This tasks have therefore often been accomplished by using various post-processing methods in which the calculation of the wall shear stress is associated with the determination of the wall position. The methods employed for the determination of the correction for the wall normal position Δy and of the boundary layer characteristic quantities will be described in this appendix. The presented algorithm has been written in MATLAB.

For both laminar boundary layer and turbulent boundary layer measurements, the integral quantities and the determination of the free stream velocity and of an initial guess of the boundary layer thickness were calculated in the same way:

```
Ue=max(U); % determination of the free stream velocity

Re=(Ue*l)/nu; % calculation of the flat plate reynolds number
```

```
Re_x=(Ue*x_coord)/nu; % // of the local reynolds number

delta_ast=trapz(y,(1-U/Ue)); % calculation of the displacement
    thickness
theta=trapz(y,(U/Ue.*(1-U/Ue))); % // of the momentum thickness
H=delta_ast/theta; % // of the form factor

Re_theta = (Ue*theta)/nu; % // calculation of the momentuum
    thickness reynolds number

y_spline=linspace(min(y),max(y),1000);  % creation of a "
    continuous" y array
U_spline=spline(y,U,y_spline);   % evaluation of the spline of
    the velocity measurements

% Determination of the boundary layer thickness...
U_cont=1;
U_curr=U_spline(U_cont);
while U_curr < 0.99*Ue
    U_curr=U_spline(U_cont);
    U_cont=U_cont+1;
end

delta=y_spline(U_cont);  %... as the coordinate where U = 0.99
    Ue
```

A.1 Post-processing of the experimental data related to laminar boundary layers

The determination of the wall shear stress and of the correction for the wall normal position Δy is much more simple for laminar boundary layers. Laminar boundary layers show a monotonic velocity profile, meaning that their shape follows a well-defined mathematical law throughout the entire boundary layer thickness, and the velocity distributions are nearly linear at moderate values of y. Furthermore, the wall shear stress is only due to viscous forces, therefore it is sufficient to apply the Newton's law for viscosity to calculate it.
In the used algorithm, the first measurement points got interpolated using a first order polynomial, then the intercept of the obtained polynomial has been used to correct the y measurements, thus representing the wall position correction Δy. In this way, the corrected experimental results will linearly go to $U = 0$ for $y = 0$. The slope of the obtained first order polynomial was instead used to determine the wall shear stress.

```
% linear interpolation of the first 5 experimental points
p = polyfit(U(1:5),y(1:5),1);
```

```
% evaluation of the y correction
delta_y = polyval(p,0);

% application of the correction
y = y - delta_y;

% evaluation of tau_w by the Newton's law
tau_ws(i) = rho*nu*p(1);
```

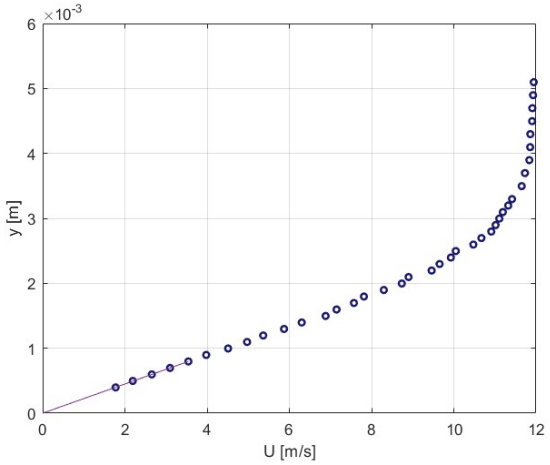

Figure A.1: Result of the y correction for a laminar boundary layer

A.2 Post-processing of the experimental data related to turbulent boundary layers

The determination of the wall shear stress and of the correction for the wall position is mush more challenging for turbulent boundary layers. The wall shear stress is defined only by viscous forces just in the viscous sublayer, whose thickness, although depending on the Reynolds number, usually is of the order of tenths of millimeters. The wall shear stress is therefore usually calculated by using methods which rely on the "wall similarity" of the velocity profiles. Some recently proposed methods are based instead on the optimization of the boundary layer parameters in order to make the inner scaled experimental data collapse on empirically determined numerical expressions of the mean velocity profiles. The post-processing algorithm used for this work employed an initial iterative optimization through the Clauser chart method [3] and a subsequent optimization trough a method recently proposed by Rodrìguez-Lòpez, Buxton and Bruce in [6].

A.2.1 Initial optimization using the Clauser chart method

The Clauser chart method is based on reporting the experimental measurements in semi-logarithmic form, normalizing the mean velocity values with the free stream velocity (U/U_∞) and the y values as yU_∞/ν. The curve of the experimental data processed in this way gets the compared with the lines produced by the following expression for different values of the skin friction coefficient c_f:

$$\frac{u}{U_e} = \sqrt{\frac{c_f}{2}} \left[\frac{1}{k} ln \left(\frac{yU_\infty}{\nu} \sqrt{\frac{c_f}{2}} \right) + B \right]$$

Where k is the Von Karman constant and B the intercept of the logarithmic region. It can be demonstrated that the line which better represent the linear segment of the experimental data (which is relative to the logarithmic region) is defined by the skin friction coefficient experienced of the measured boundary layer.
The Clauser chart method was applied iteratively by correcting the y measurements at every iteration to make one of the measured points coincide to the theoretical logarithmic law. The results obtained with the Clauser chart method was used to provide an initial guess of the friction velocity u_τ, which was calculated from the c_f values, and of the wall position correction, thus serving as a starting point for the next optimization phase.

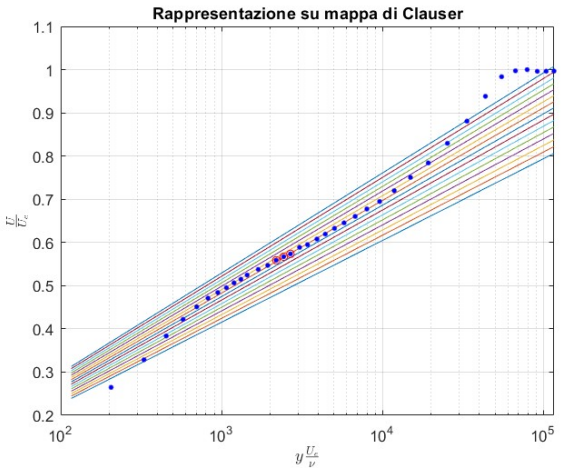

Figure A.2: Application of the Clauser chart method to the experimental data

A.2.2 Optimization algorithm

After obtaining a first guess of u_τ and c_f through the Clauser chart method, a further optimization algorithm was applied. The employed algorithm is based on the optimization of 5 parameters u_τ, Δy, k, δ and Π. Those parameters

get optimized in such a way that the experimental data collapses on a velocity profile defined by three components. These are the Musker's profile [24], which consists in a continuous description of the viscous sublayer, buffer layer and logarithmic layer, a bump component, which describes the velocity profile's bump at the end of the overlap region and a wake component, which describes the outer part of the velocity profile.

The Musker's profile is defined as follows:

$$\frac{\partial u^+}{\partial y^+} = \frac{\frac{(y^+)^2}{k} + \frac{1}{s}}{(y^+)^3 + \frac{(y^+)^2}{k} + \frac{1}{s}};$$

Where s is a constant which has the effect of changing the intercept of the logarithmic law, B [6]. The determination of u^+_{musker} involved the resolution of a differential equation, which was solved by applying the explicit Euler's method.

The ending bump of the logarithmic region is described by an overshoot of the following expression, which was found by Monkewitz [28]:

$$u^+_{bump} = \frac{1}{M_2} exp\left[-Log^2\left(\frac{y^+}{M_1}\right)\right];$$

Were $M_1 = 30$ and $M_2 = 2.85$.

And the wake component, which has been described in [19] is defined as:

$$W(\eta) = \frac{1 - exp\left[-\frac{1}{4}(5a_2 + 6a_3 + 7a_4)\eta^4 + a_2\eta^5 + a_3\eta^6 + a_4\eta^7\right]}{1 - exp(-\frac{1}{4}(a_2 + 2a_3 + 3a_4))}\left(1 - \frac{1}{2\Pi} ln(\eta)\right)$$

Where $\eta = y/\delta$, $a_2 = 132.8410$, $a_3 = 166.2041$, and $a_4 = 71.9114$.

The "canonical" u^+ profile is then defined by the sum of the three different components for $0 < y^+ < \delta^+$:

$$u^+ = u^+_{musker} + u^+_{bump} + \frac{2\Pi}{k} W(\eta)$$

And as $u^+ = U^+_\infty$ for $y^+ > \delta^+$.

The function to minimize by optimizing the previously listed variables is the error of the experimental data with respect to the "canonical" profile and will be composed of two error components.

- The mean relative error, which will give greater weighting to the experimental data measured closer to the wall [6]:

$$E_1(u_\tau, \Delta y, k, \delta, \Pi) = \left\langle \frac{\left|u^+_{canonical} - u^+_{experimental}\right|}{u^+_{canonical}} \right\rangle$$

- The mean quadratic error which will consider all the points of the velocity profile equally [6]:

$$E_(u_\tau, \Delta y, k, \delta, \Pi) = \left\langle \sqrt{(u^+_{canonical} - u^+_{experimental}} \right\rangle$$

The two error components have been added together, giving $E = E_1 + E_2$.
The problem was solved through sequential quadratic programming (sqp) using the "*fmincon*" MATLAB function.
The intercept of the logarithmic region, B, was finally determined by integrating with Newton Rhapson's method the following experimental relation given by Nagib and Cauhan [13]:

$$kB = 1.6exp[(0.1663B) - 1]$$

MATLAB code of the error function:

```
function E = error(x, y_real, u_real, nu)
    u_tau = x(1);  % extraction of u_tau from the array of the
       variables
    delta_y = x(2); % // of delta_y //
    k = x(3); % // of k //
    Pi = x(4); % // of Pi //
    delta = x(5); % // of delta //

    y = y_real+delta_y; % correction of y through delta_y
    y_plus = (y)*u_tau/nu; % normalization of y with u_tau
    u_plus = u_real./u_tau; % normalization of u with u_tau

    % musker's profile definition
    s = 0.001393; % Definition of the s constant
    y_plus_0 = 0; % initialization of the first grid point for
       the Euler's method
    y_plus_N = round(y_plus(end),3); % // last grid point //

    % definition of the musker's differential equation
    f = @(y_plus,u) (y_plus.^2/k + 1/s) ./ (y_plus.^3 + y_plus
       .^2/k + 1/s);

    u0 = 0;
    step = 0.01; % definition of the Euler's method step length
    y_plus_cont = 0:step:y_plus_N; % definition of the Euler
       method's grid points
    N = length(y_plus_cont)-1;

    % application of the Euler's method
    full_musker = eulero_espl(f, y_plus_0, y_plus_N, u0, N)';

    % calculation of u_musker in the experimental measurement's
        positions
```

```
    u_plus_musker = spline(y_plus_cont, full_musker, y_plus);

    % definition of the bump component
    M1 = 30;
    M2 = 2.85;
    u_plus_bump = 1/M2*exp(-(log10(y_plus/M1)).^2);

    % definition of the wake function
    a2 = 132.8410;
    a3 = -166.2041;
    a4 = 71.9114;

    eta = y/delta;

    numerator = 1 - exp(- (1/4) * (5*a2 + 6*a3 + 7*a4) * eta.^4
        + a2*eta.^5 + a3*eta.^6 + a4*eta.^7);
    denominator = 1 - exp(- (1/4) * (a2 + 2*a3 + 3*a4));
    log_term = 1 - 1/(2*Pi) * log(eta);

    W = (numerator ./ denominator) .* log_term;

    % definition of the wake velocity component
    u_plus_wake = 2*Pi./k*W;

    % definition of u_canonical for y<delta
    u_plus_int = u_plus_musker(y <= delta) + u_plus_bump(y <
       delta) + u_plus_wake(y < delta);

    % definition of u_canonical for y>delta
    u_plus_ext = ones(1, length(y(y > delta)))*u_plus_int(end);

    % definition of u_canonical
    u_plus_can = [u_plus_int, u_plus_ext];

    % error evaluation
    E = mean(abs(u_plus_can-u_plus)./u_plus_can)+mean(sqrt((
       u_plus_can-u_plus).^2));
end
```

Error initialization and setting of the optimization algorithm:

```
% Define the error function E
E = @(x) error(x, y, U , nu);

% Initial guesses
u_tau_in = u_tau;

% Set initial parameter vector x0
x0 = [u_tau_in, 0, 0.385, 0.5, delta];
```

```
% Lower bounds for optimization
Low = [0.5 * u_tau_in, -y(1) , 0.36, 0 , 0.8 * delta];

% Upper bounds for optimization
Up = [1.5 * u_tau_in, y(1), 0.4, 2, 1.8 * delta];

% Define optimization options
options = optimoptions("fmincon", "Algorithm", "sqp", ...
    "MaxFunctionEvaluations", 1.0e5, ...
    "OptimalityTolerance", 1.0e-10, ...
    "StepTolerance", 1.0e-16, ...
    "ConstraintTolerance", 1.0e-10, ...
    "Display", "iter");

% initialization of the error
E_initial = E(x0);

fprintf("Initial error value: %f\n", E_initial);

% Perform optimization using fmincon
[x, ~, exitflag] = fmincon(E, x0, [], [], [], [], Low, Up, [],
   options);
```

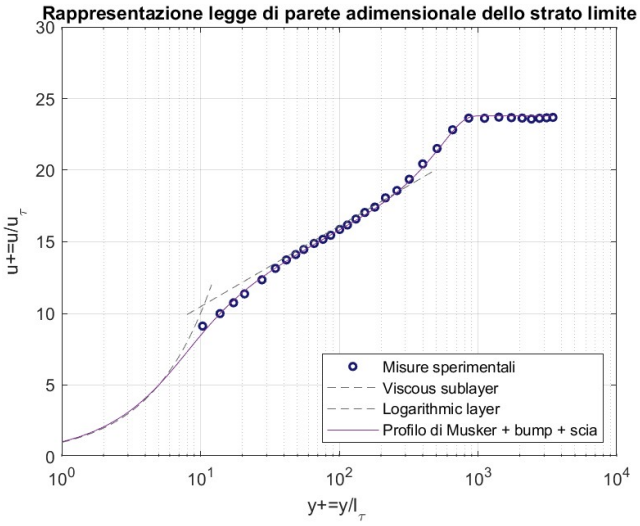

Figure A.3: Result of the optimization of the parameters

A.2.3 Modification of the algorithm for the riblet manipulated boundary layers

Riblets manipulate the turbulent boundary layer by shifting the mean streamwise velocity profiles away from the wall. In particular, Garcia Mayoral and

Garcìa-Mayoral and J. Jimenéz [10] have explained that the intercept of the logarithmic layer gets incremented by a ΔB when riblets produce drag reduction. They also stated that, conversely, the other parameters which describe the velocity profile are not modified by riblets. For this reason, the previously described optimization algorithm has been modified to allow the optimization of the parameters in the case of riblet-manipulated turbulent boundary layers. This was done by fixing the k and Π constants at the values obtained for the boundary layers measured over the smooth plate at the same flow regime and by giving the algorithm the freedom to vary the value of the s constant of the Musker's profile, which is responsible for the variation of B. This modified algorithm is therefore absolutely analogous to the previously described one, but uses u_τ, Δy, δ and s as optimization variables.

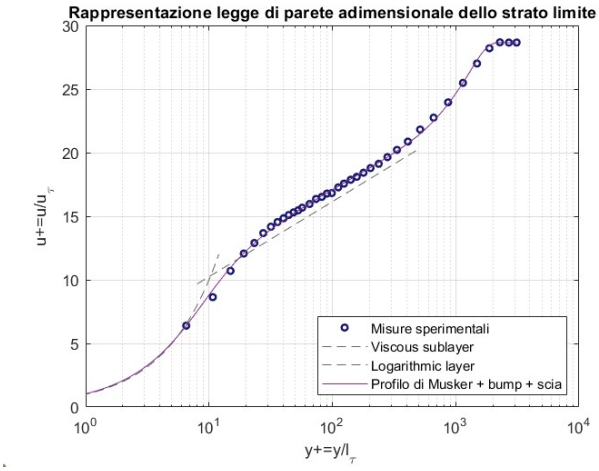

Figure A.4: Result of the optimization of the parameters for a riblet manipulated turbulent boundary layer

Bibliography

[1] S.Discetti C. Sanmiguel Vila R. Vineusa et al. “On the identification of well-behaved turbulent boundary layers”. In: *Jurnal of fluid mechanics* (2017).

[2] C.B.Millikan. “Proceedings of the Fifth International Congress of applied Mechanics”. In: *A critical discussion of turbulent flows in channels and circular tubes.* 1938.

[3] F.H. Clauser. “Turbulent boundary layers in adverse pressure gra dients”. In: *J. Aerosp. Sci.* (1954).

[4] L.Sirovich D.B. Goldstein R. Handler. “Direct numerical simulation of turbulent flow over a modeled riblet covered surface”. In: *Journal of Fluid Mechanics* (1995).

[5] G. Hoppe D.W. Bechert M. Bartenwerfer and W.-E. Reif. “Drag reduction mechanisms derived from shark skin”. In: *Proceedings of the 15th Congress of the International Council of the Aeronautical Sciences, 7–12 September 1986, London.* 1986.

[6] P. J. K. Bruce E. Rodrìguez-Lòpez and O.R.H. Buxton. “A robust post-processing method to determine skin friction in turbulent boundary layers from the velocity profile”. In: *Experiments in Fluids* (2015).

[7] P. J. K. Bruce E. Rodrìguez-Lòpez and O.R.H. Buxton. “Near field development of artificially generated high Reynolds number turbulent boundary layers”. In: (2016).

[8] G. Iuso G. Cafiero. “Drag reduction in a turbulent boundary layer with sinusoidal riblets”. In: (2022).

[9] G. Iuso G. Cafiero and E. Amico. “Manipulation of a turbulent boundary layer using sinusoidal riblets”. In: (2024).

[10] R. Garcìa-Mayoral and J. Jimenéz. “Drag reduction by riblets”. In: (2011).

[11] J. Kim H. Choi P.Moin. “Direct numerical simulation of turbulent flow over riblets”. In: *Journal of Fluid Mechanics* (1993).

[12] P.J. Finleyt H.H. Frenholz. “The incompressible zero-pressure-gradient turbulent boundary layer: An assessment of the data”. In: *Progress in Aerospace Sciences* (1996).

[13] K.A Chauhan H.M Nagib. “Variations of von Karman coefficient in canonical flows”. In: *Physics of Fluids* (2008).

[14] S. Balachandar J. Zhou R.J. Adrian and T. M. Kendall. “Mechanisms for generating coherent packets of hairpin vortices in channel flow”. In: *Journal of Fluid Mechanics* (1999).

[15] R. F. Blackwelder J.D.Swearingen. “The growth and breakdown of streamwise vortices in the presence of a wall”. In: *Journal of Fluid Mechanics* (1987).

[16] J.Osterlund. “Experimental Studies of Zero Pressure-Gradient Turbulent Boundary-Layer Flow”. PhD thesis. Royal Institute of Technology. Stockholm,Sweden, 1999.

[17] J.Szodruch. “Viscous drag reduction on transport aircraft”. In: *AIAA paper 91-0685*. 1991.

[18] J. Jimenéz. “Near-wall turbulence”. In: *Physics of Fluids* (2013).

[19] P. A. Monkewitz K. A. Chauhan and H. M. Nagib. “Criteria for assessing experiments in zero pressure gradient boundary layers”. In: *Fluid dynamics research* (2009).

[20] T. von Kármán. “Turbulence and Skin Friction”. In: *Journal of the Aeronautical Sciences* (1934).

[21] L.Prandtl. “Zur turbulenten Stromung in Rohren und langs Platten.” In: Ergebn. Aerodyn. Versuchsanst. Gottingen, 1932, pp. 18–29.

[22] A. Lindemann M. Walsh. “Optimization and application of riblets for turbulent drag reduction”. In: *AIAA paper 84-0347*. 1984.

[23] G. Marchesano. “Progetto e caratterizzazione di un sistema di misura per la resistenza aerodinamica basato su LVDT”. MA thesis. Politecnico di Torino, 2024.

[24] A. Musker. “Explicit expression for the smooth wall velocity dis tribution in a turbulent boundary layer”. In: *AIAA journal* (1979).

[25] M. Ewenz Rocher O. R. H. Buxton and E. Rodrìguez-Lòpez. “The inuence of strong perturbations on wall-bounded flows”. In: (2018).

[26] R. Orlu P. H. Alfredsson A. Segalini. “A new scaling for the streamwise turbulence intensity in wall-bounded turbulent flows and what it tells us about the “outer” peak”. In: *Physics of Fluids* (2011).

[27] A.Pozzi P. Luchini F. Manzo. “Resistance of a grooved surface to parallel flow and cross-flow”. In: *Journal of Fluid Mechanics* (1991).

[28] H.M. Nagib P.A. Monkewitz K. A. Chauhan. “Self-consistent high reynolds-number asymptotics for zero-pressure-gradient turbu lent boundary layers”. In: *Physics of Fluids* (2007).

[29] R. Pietropaolo. “Ammodernamento e caratterizzazione di una galleria del vento per studio dello strato limite”. MA thesis. Politecnico di Torino, 2024.

[30] S.K. Robinson. “Coherent motions in the turbulent boundary layer”. In: *Annual review of fluid mechanics* (1991).

[31] S.K.Robinson. “The kinematics of turbulent boundary layer structure”. PhD thesis. Stanford University, 1990.

[32] F. Hussein W.Schoppa. “Coherent structure dynamics in near-wall turbulence”. In: *Fluid dynamics research* (2000).

[33] N. Kasagi Y. Suzuki. “Turbulent drag reduction mechanism above a riblet surface”. In: *AIAA Journal* (1994).

Acknowledgments

I would like to express my gratitude to Prof. Cafiero and Prof. Serpieri for giving me the opportunity to work on this stimulating project, which has allowed me to significantly expand my understanding of experimental fluid-dynamics and beyond. I am deeply grateful to Edoardo Fracchia for the constant support he gave me through this journey; His help was fundamental for completing this work. I would also like to thank Prof. Iuso for the precious advice he shared, drawing from his vast experience. I wish to extend my thanks to all the PhD students and undergraduate thesis students at the laboratory, for fostering such a stimulating and collaborative environment, while also making every workday enjoyable.

My deepest gratitude goes to all of my family, to whom this thesis is dedicated. They always supported my choices without any hesitation and done everything possible to help me pursue my studies. In particular, I would like to thank my mother: her constant and unwavering encouragement has been indispensable in reaching this milestone. My father, who instilled in me both a strong work ethic and practical knowledge that became fundamental to this work; even some of the tools we used in our summertime projects found unexpected applications and always surprised everyone in the lab. Davide, who shared nearly every moment of my academic journey: you were always there to cheer me up during challenges but also to celebrate each milestone I achieved. I hope I have reciprocated by helping you pursuing your journey up to this moment and I promise to continue with the same dedication. Finally, my grandparents and all the rest of my family: the pride you have shown towards me, which I often considered more generous than deserved, became the motivation that pushed me to always give my best in my studies.

I would then like to thank my friends and study colleagues: Alessandro, Daniele, Davide, Erica, Giacomo, Matteo, Sebastiano and Stella; Having met you was truly crucial in elevating my university experience during the master's degree. We collaborated in numerous group projects, often improbable ones, and supported each other during our study sessions. Our outings perfectly

complemented my academic experience providing much needed brakes from studying.

My gratitude also goes to my lifelong friends who have always been on my side since high school years. To Bassa, Modu, Nengo, Soos and Weili: our night outs and vacations allowed me to relive the carefree days spent behind the desks of the *"Curie"* and to recharge and gather the energy to start each academic year. To Giulia, Nova, and Pierre: the dinners and parties we spent together have always been an opportunity not only for leisure but also to support each other on our careers paths.

"Vorrei ringraziare i Professori Cafiero e Serpieri per avermi dato l'opportunità di svolgere questo stimolante progetto, che mi ha permesso di incrementare le mie conoscenze nell' aerodinamica sperimentale e non solo. Sono profondamente grato ad Edoardo Fracchia, che mi ha fornito un supporto costante durante questo percorso; Il suo aiuto è stato fondamentale per completare questo progetto. Vorrei anche ringraziare il Professor Iuso per i preziosi consigli che ha condiviso con me grazie alla sua esperienza. Desidero estendere questi ringraziamenti a tutti gli studenti di dottorato e tesisti del laboratorio per aver creato un ambiente stimolante e di collaborazione, rendendo allo stesso tempo piacevole ogni giornata di lavoro.

Il mio ringraziamento più sentito va a tutta la mia famiglia, a cui questa tesi è dedicata. Avete sempre supportato ogni mia scelta senza esitazione e fatto tutto il possibile perché potessi perseguire i miei studi nel migliore dei modi. Vorrei ringraziare mia mamma, i cui instancabili incoraggiamenti sono stati indispensabili per raggiungere questo traguardo. Mio papà, che mi ha trasmesso sia la disciplina nel lavoro sia alcune conoscenze pratiche che si sono inaspettatemente rivelate fondamentali in questo progetto; persino alcuni degli attrezzi che abbiamo usato per i nostri lavori di casa estivi si sono dimostrati utili in questo lavoro, sorprendendo sempre tutti. Davide, con il cui ho condiviso la maggior parte delle mie giornate durante il mio percorso accademico: ci sei sempre stato quando ho avuto bisogno di supporto durante le difficoltà ma anche per festeggiare i miei traguardi. Spero di aver ricambiato aiutandoti nel tuo percorso e prometto che continuero a farlo con lo stesso impegno. Infine, i miei nonni e tutto il resto della mia famiglia: l'orgoglio che avete sempre dimostrato nei miei confronti, che io ho spesso considerato esagerato, si è trasformato nella motivazione che mi ha spinto a dare sempre del mio meglio nei miei studi.

Vorrei poi ringraziare i miei amici e compagni di corso: Alessandro, Daniele,

Davide, Erica, Giacomo, Matteo, Sebastiano e Stella; Avervi conosciuto è stato veramente importante nel migliorare la mia sperienza universitaria durante la magistrale. Abbiamo collaborato in diversi lavori di gruppo, spesso improbabili, e ci siamo aiutati a vicenda durante le nostre giornate in aula studio. Le nostre uscite hanno completato perfettamente l'esperienza accademica, regalandomi attimi di distrazione dallo studio.

Il mio ringraziamento va poi ai miei amici di sempre, quelli che ci sono sempre stati fin dagli anni del liceo. A Bassa, Modu, Nengo, Soos e Weili: le serate insieme e le nostre vacanze estive mi hanno fatto rivivere la spensieratezza dei giorni passati dietro ai banchi del "Curie" e permesso di ricaricare le energie per ricominciare ad ogni nuovo anno accademico. A Giulia, Nova e Pierre: le cene e feste passate insieme sono state un'ulteriore fonte di svago ma anche occasioni per confrontarci sui nostri percorsi."